# Particle Identification and Data Analysis - II

Kétévi Adiklè Assamagan

Brookhaven National Laboratory

Abstract

In the first part of this lecture, we will review the techniques on which
particle physics detectors are based, taking as concrete example,
the ATLAS and CMS detectors at the LHC. In the second part, we will
address basic object identifications with particle physics detector. In
the last part of the lecture, we will study applications to searches at the LHC.
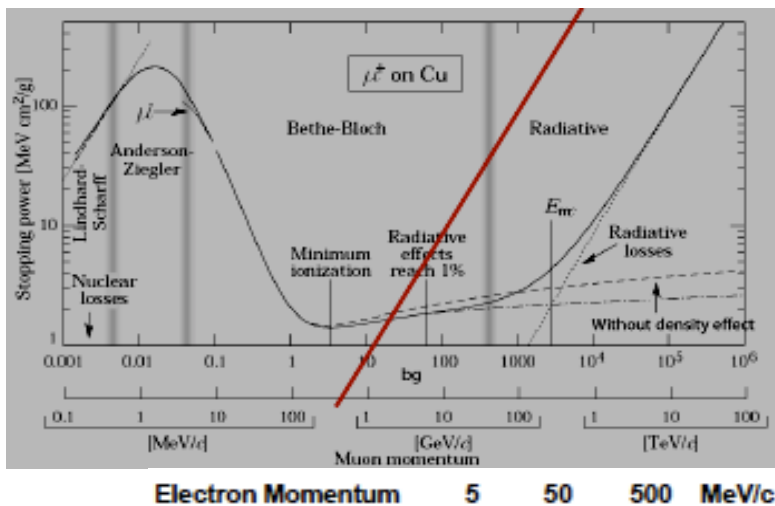
Recall – from Part I

Bremsstrahlung: a charged particle of mass M and charge $q=Z_1 e$ is deflected by a nucleus of charge Ze which is partially shielded by atomic electrons. During the deflection, the charge is accelerated and therefore radiates
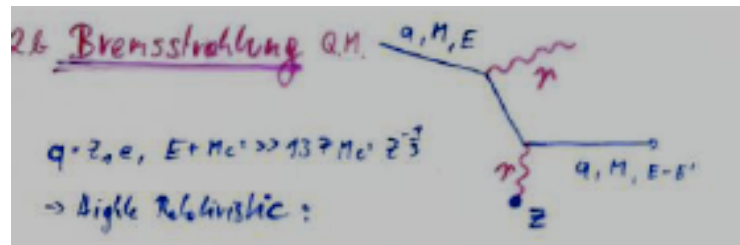
Proportional to Z^2/A of material
Proportional to Z_1^4 of incoming particle
Proportional to $1/M^2$ of particle
Proportional to the Energy of particle: $E(x)=E_0 exp(-x/X_0)$
X_0 = radiation length

Critical Energy:
dE/dx(Ionization) = dE/dx (Bremsstrahlung)

Pair Production: photon conversion into $e^- e^+$ pair in a material

For $E\gamma >> m_e C^2 = 0.5$ MeV; $\lambda = 9/7 X0$. The average distance a photon travels before it converts into an e+e- pair is equal to 9/7 of the distance an electron travels before reducing its energy from E_0 to $E_0 exp(-1)$ by brem

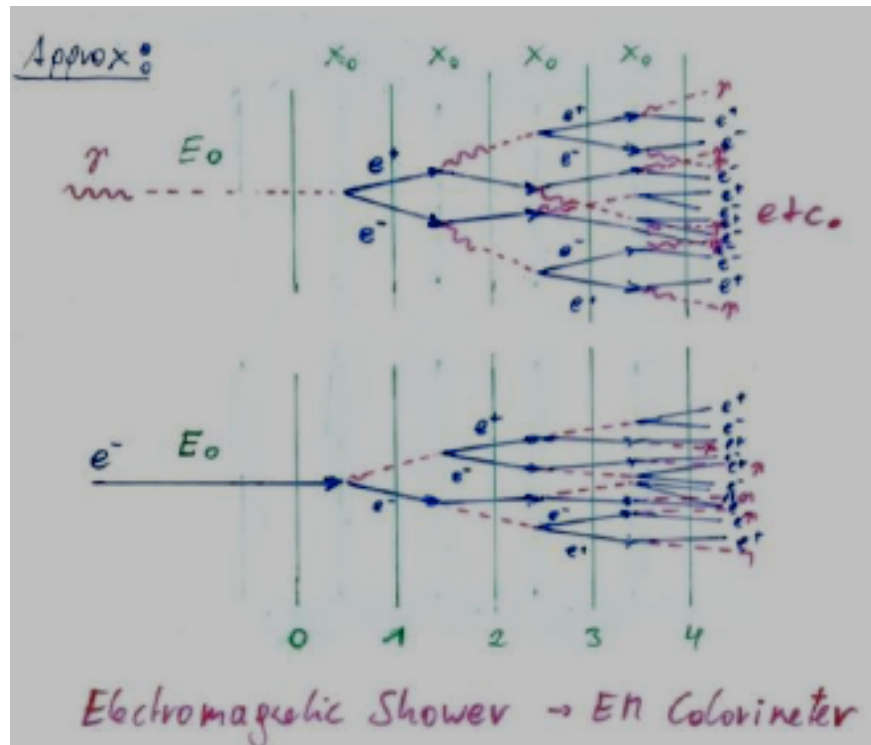**Electron Momentum   5   50   500 MeV/c**

For muon, second lightest particle after electron, critical energy is at 400 GeV. EM brem is only relevant for electrons at energies of present detectors

2

Recall – from Part I

Approx:

Electromagnetic Shower → EM Calorimeter
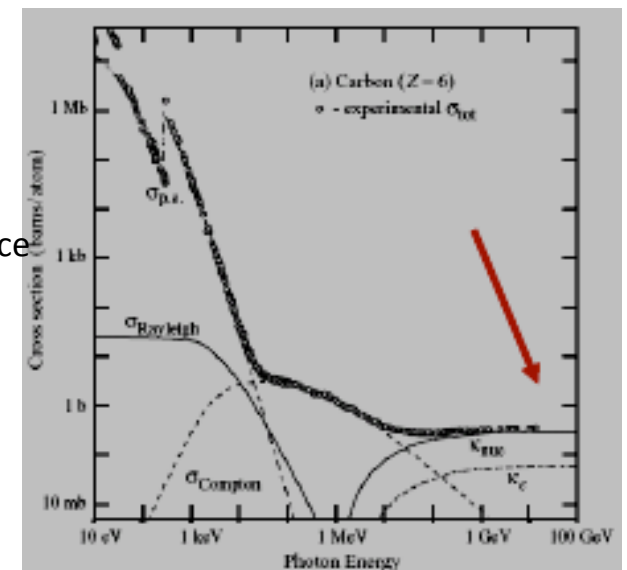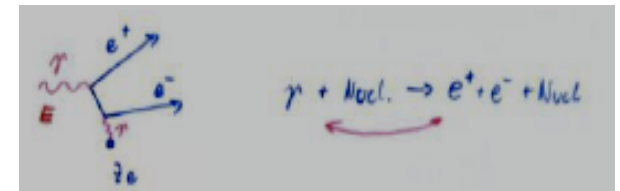
$N(n) = 2^n$ ..... Number of particles $(e^\pm, \gamma)$ after $n X_0$

$E(n) = \dfrac{E_0}{2^n}$ .... Average Energy of particles after $n X_0$

Shower stops if $E(n) = E_{critical}$

$\Rightarrow n_{max} = \dfrac{1}{\ln 2} \ln \dfrac{E_0}{E_c}$ → Shower length rises with $\ln E_0$

Number of $e^\pm$ track segments (of length X_0) after $n X_0$:
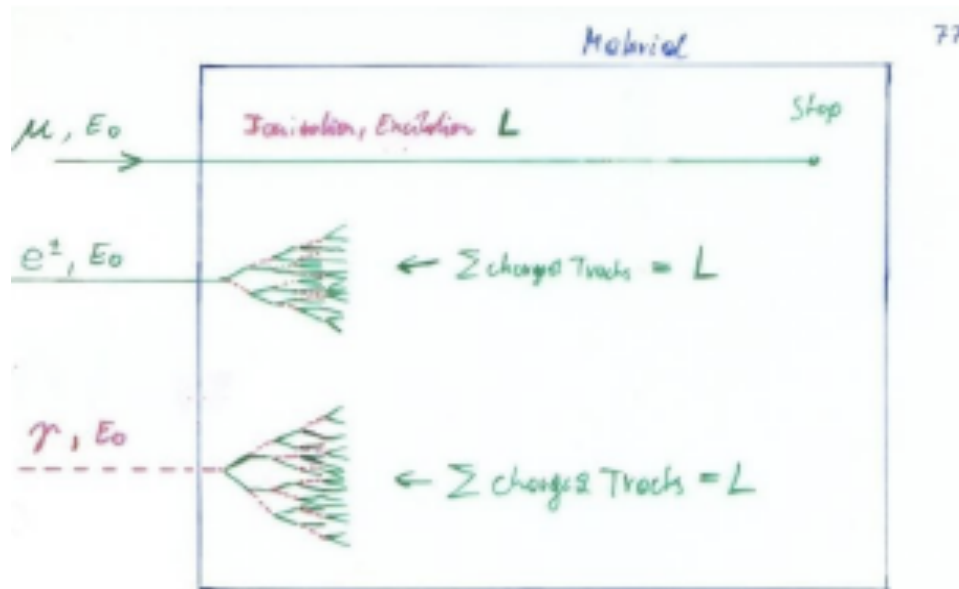
$$N_{tr}(n) = 2^n$$

Total $e^\pm$ track length (after $n_{max} X_0$)

$$L = \sum_{n=0}^{n_{max}} 2^n X_0 = \left(2 \frac{E_0}{E_c} - 1\right) X_0 \sim 2 \frac{E_0}{E_c} X_0 = c_1 \cdot E_0$$

Total (charge) track length is proportional to the Energy of the Particle.

→ Calorimeter Principle

3

Calorimeters: Energy measurement by total absorption of the incoming particle

Material   77

μ, E_0 → Ionization, Excitation L   Stop

$e^\pm, E_0$ ← Σ charged Tracks $= L$

γ, E_0 ← Σ charged Tracks $= L$

The $e^\pm$ in the Calorimeter ionize and excite the material

Ionization: e^-, I^+ pairs in the material

Excitation: Photons in the material

Measuring the total Number of e^-, I^+ pairs or the total Number of Photons gives the particle Energy.

If N is the total Number of e^+, I^+ pairs or photons, or $N = c_1 E_0$:

$\Delta N = \sqrt{N}$ (Poisson Statistics)

$$\frac{\Delta E}{E} = \frac{\Delta N}{N} = \frac{1}{\sqrt{N}} = \frac{a}{\sqrt{E}} \rightarrow \text{Resolution}$$

Only Electrons and High Energy Photons show EM cascades at current GeV-TeV level Energies.

Strongly interacting particles like Pions, Kaons, produce hardonic showers in a similar fashion to the EM cascade →Hadronic calorimetry

4

Calorimeters: Energy measurement by total absorption of the incoming particle

The Measurement is destructive. The particle can not be subject to further study.

Energy Measurement by
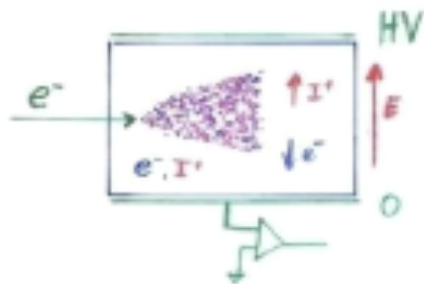
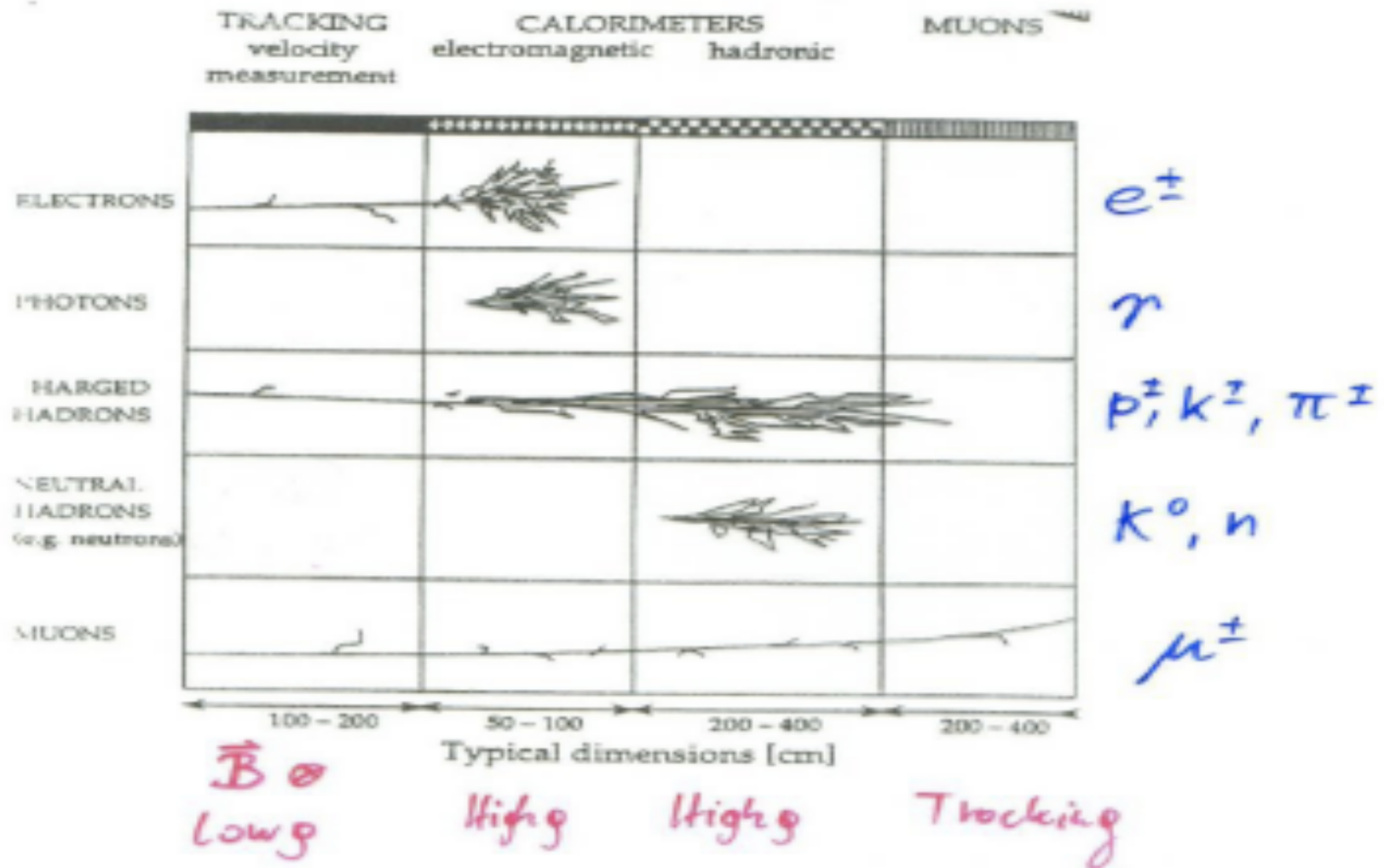Collecting the produced Charge

Liquid Nobel Gases (Nobel Liquids)

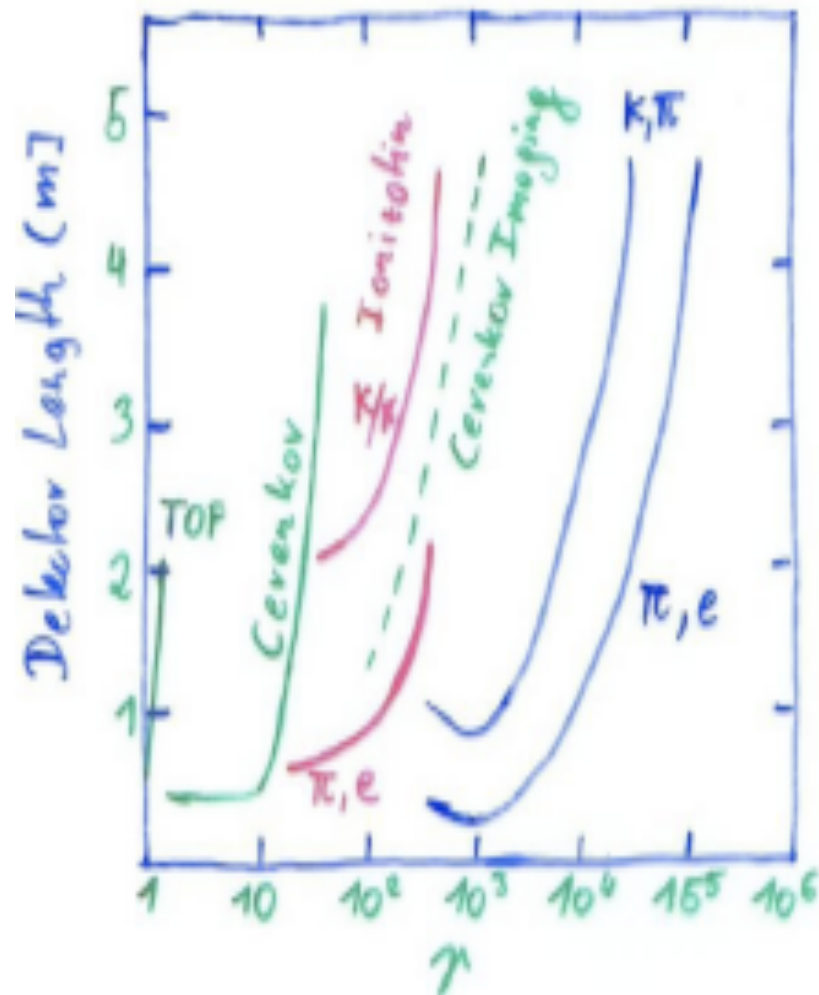Measuring the Photons produced by the collision of the $e^{\pm}$ with Atom electrons of the Material.

Scintillating Crystals, Plastic Scintillators

Total Amount of e^-, I^+ pairs or Photons is proportional to the total track length is proportional to the particle Energy.
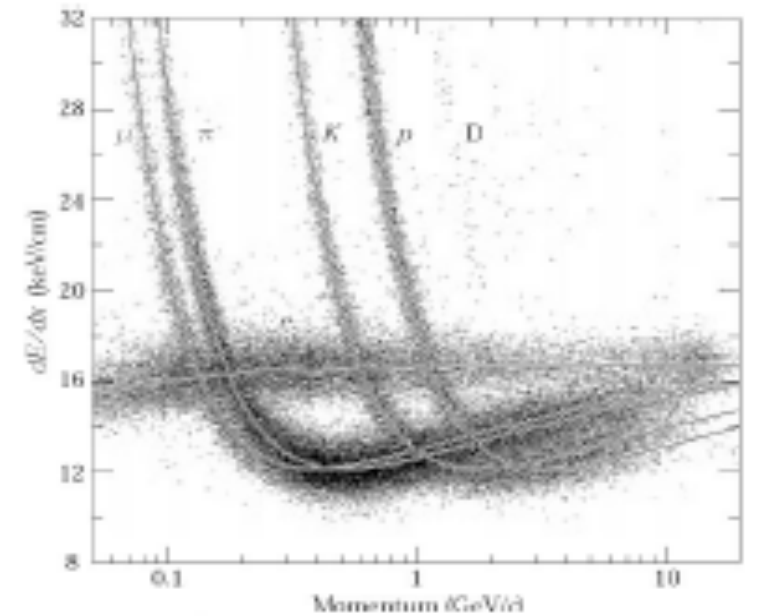
Particle Identification

Particle Identification

1) • For low Energies the Time of Flight (TOF) measures the Velocity $p, v \to m$

2) • For longer Energies the Cerenkov Threshold $v > \frac{c}{n}$ discriminates between Particles

3) • For $\gamma \sim 100$ the multiple $\frac{dE}{dx}$ measurements provide Identification

4) • Cerenkov Angle Measurements $\cos\theta = \frac{1}{n\beta}$ provide Particle ID

5) • At very high γ the Transition Radiation allows Identification

dE/dx
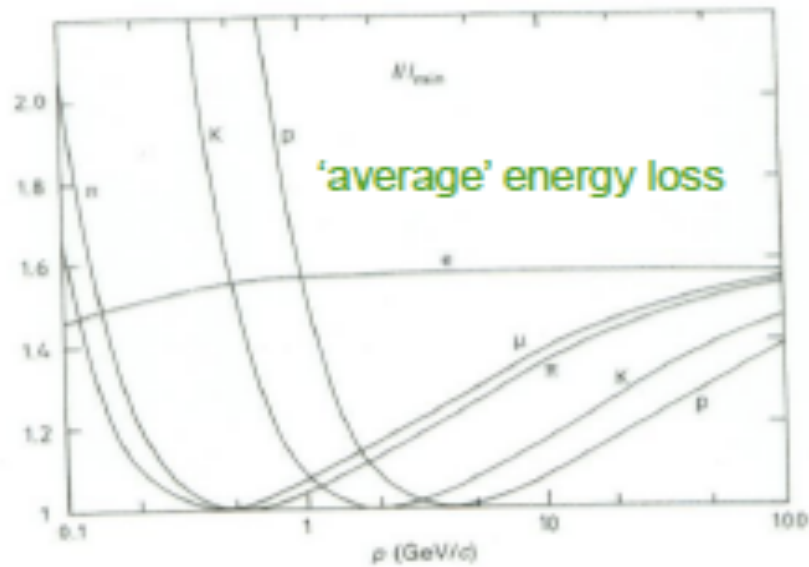
'average' energy loss

In certain momentum ranges, particles can be identified by measuring the energy loss.
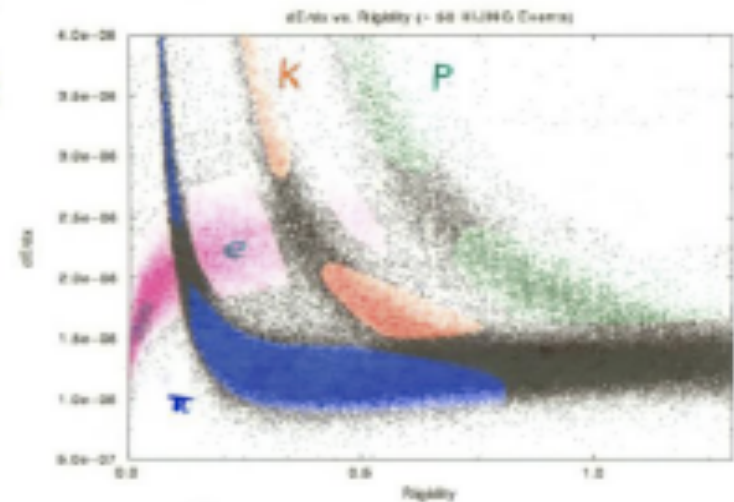
STAR TPC

Time of Flight (TOF)

t_0

t_2

π, k

E.g : $D = 2m$, $\sigma_t = 100\,ps$ $(10^{-40}s)$

3σ Significance $\rightarrow$ $T = t_2 - t_1 \geq 300\,ps$

$p = m v \cdot \gamma \rightarrow v = \dfrac{c}{\sqrt{1 + \frac{m^2 c^2}{p^2}}}$, $T = \dfrac{D}{v}$

$T = \dfrac{D}{c}\sqrt{1 + \frac{m^2 c^2}{p^2}}$

TOF Difference 1_m (ps)

TOF Difference 2_m (ps)

700
600
500
400
300
200
100

π/p

π/k

k/p

1400
1200
1000
800
600
400
300
200

0.5   1   1.5   2   2.5   3   3.5 $p\,[\frac{GeV}{c}]$
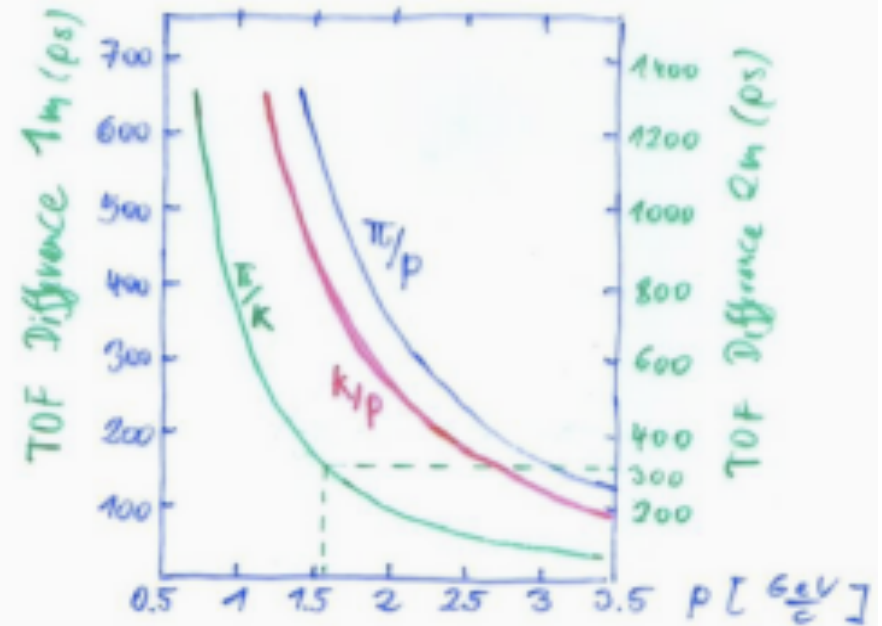
NA49 combined particle ID: TOF + dE/dx (TPC)

e^+ π^+

k^+ p

Entries

4000
3000
2000
1000
0

1.4   1.2   1.0   0.8

dE/dx

1.5   1   0.5   0   -0.5

$m^2\,(GeV^2)$

TPC dE/dx vs TOF p=+1 GeV/c

TOF [TDC CH]

700
600
500
400
300

p

π

μ

$1.5\,GeV/c$

40
35
30
25
20
15
10
5

0   100   200   300   400   500

TPC dE/dx [ADC CH]
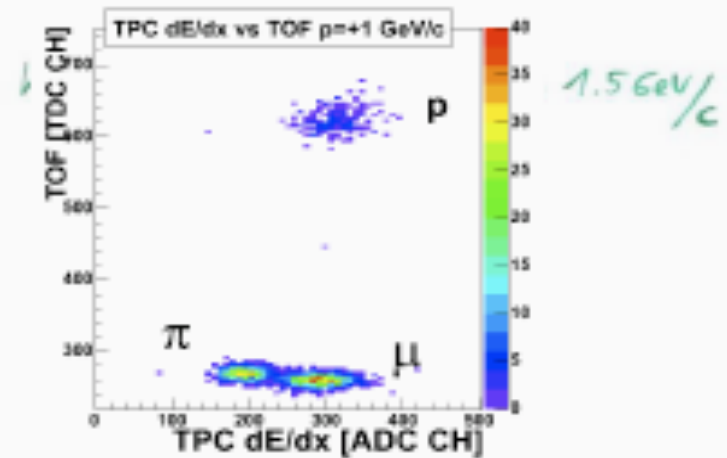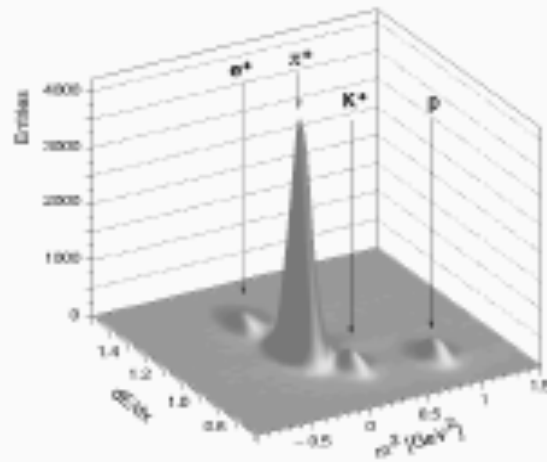
Cherenkov Radiation

If the velocity of a charged particle is larger than the velocity of light in the medium $v > \frac{c}{n}$ (n... Refractive Index of Material)

it emits 'Cerenkov' radiation at a characteristic angle of $\cos\theta_c = \frac{1}{n\beta}$ $(\beta = \frac{v}{c})$

$$\frac{dN}{dx} \approx 2\pi\alpha\, z_1^2 \left(1 - \frac{1}{\beta^2 n^2}\right) \frac{\lambda_2 - \lambda_1}{\lambda_2 \cdot \lambda_1}$$

• Number of emitted Photons/length with λ between λ_1 and λ

With $\lambda_1 = 400\,nm$ $\lambda_2 = 700\,nm$

$$\frac{dN}{dx} = 490 \left(1 - \frac{1}{\beta^2 n^2}\right) \left[\frac{1}{cm}\right]$$

Material	n-1	β threshold	γ threshold
solid Sodium	3.22	0.24	1.029
lead glass	0.67	0.60	1.25
water	0.33	0.75	1.52
Silica aerogel	0.025-0.075	0.93-0.976	2.7 - 4.6
air	$2.93 \cdot 10^{-4}$	0.9997	41.2
He	$3.3 \cdot 10^{-5}$	0.99997	123

Ring Imaging Cherenkov (RICH) detectors

$\cos\theta = \frac{1}{n\beta}$

~ UV Photons

Detector

Mirror (Spherical)

Gas

$200 \frac{GeV}{c} \; k, \pi$

Resolution $\frac{\Delta \gamma}{\gamma} = \gamma^2 \beta^3 n \, \Delta\theta \frac{1}{\sqrt{N_0 L}}$ $\left(\gamma = \frac{1}{\sqrt{1-\gamma^2}}\right)$

Angle Measurement accuracy

Photon Statistics

Ring Radius [mm]

test beam data
p = 2 GeV/c

σ = 12.8 mrad

σ = 15.2 mrad

protons

pions

Single Cherenkov angle (rad)

ATLAS Inner Detector

6.2m

2.1m

Barrel semiconductor tracker
Pixel detectors
Barrel transition radiation tracker
End-cap transition radiation tracker
End-cap semiconductor tracker

Figure 1.2: Cut-away view of the ATLAS inner detector.

Table 1.2: Main parameters of the inner-detector system.

| Item		Radial extension (mm)	Length (mm)
Overall ID envelope		$0 < R < 1150$	$0 < |z| < 3512$
Beam-pipe		$29 < R < 36$	
Pixel	Overall envelope	$45.5 < R < 242$	$0 < |z| < 3092$
3 cylindrical layers	Sensitive barrel	$50.5 < R < 122.5$	$0 < |z| < 400.5$
2×3 disks	Sensitive end-cap	$88.8 < R < 149.6$	$495 < |z| < 650$
SCT	Overall envelope	$255 < R < 549$ (barrel)	$0 < |z| < 805$
		$251 < R < 610$ (end-cap)	$810 < |z| < 2797$
4 cylindrical layers	Sensitive barrel	$299 < R < 514$	$0 < |z| < 749$
2×9 disks	Sensitive end-cap	$275 < R < 560$	$839 < |z| < 2735$
TRT	Overall envelope	$554 < R < 1082$ (barrel)	$0 < |z| < 780$
		$617 < R < 1106$ (end-cap)	$827 < |z| < 2744$
73 straw planes	Sensitive barrel	$563 < R < 1066$	$0 < |z| < 712$
160 straw planes	Sensitive end-cap	$644 < R < 1004$	$848 < |z| < 2710$

1.2 Tracking

Approximately 1000 particles will emerge from the collision point every 25 ns within $|\eta| < 2.5$, creating a very large track density in the detector. To achieve the momentum and vertex resolution requirements imposed by the benchmark physics processes, high-precision measurements must be made with fine detector granularity. Pixel and silicon microstrip (SCT) trackers, used in conjunction with the straw tubes of the Transition Radiation Tracker (TRT), offer these features.

The Inner Detector is immersed in 2T magnetic field generated by a central Solenoid which extends over a length of 5.3 m with a diameter of 2.5 m

ATLAS Calorimeter
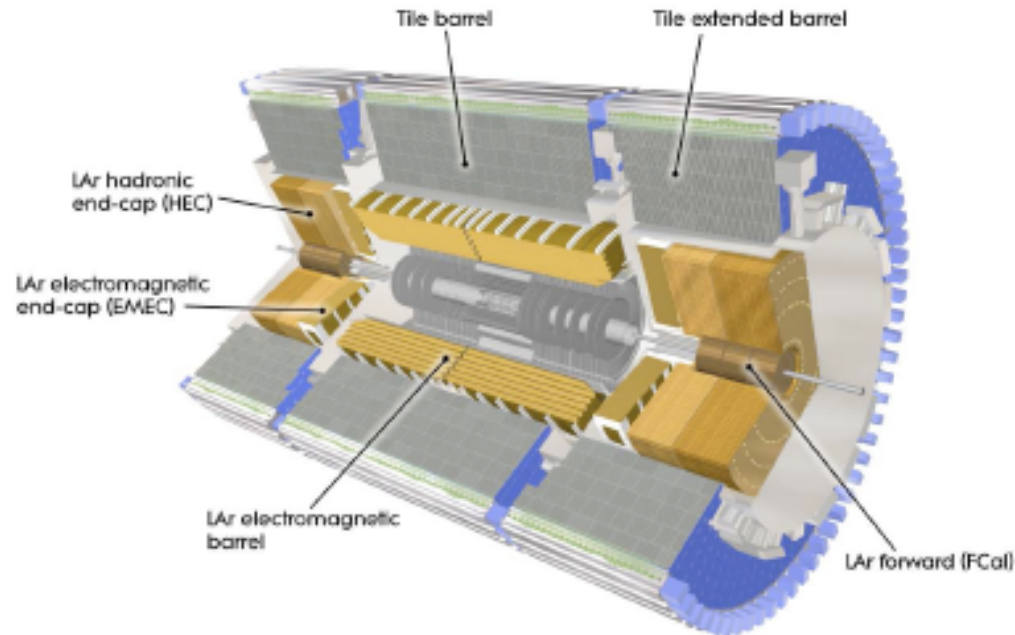
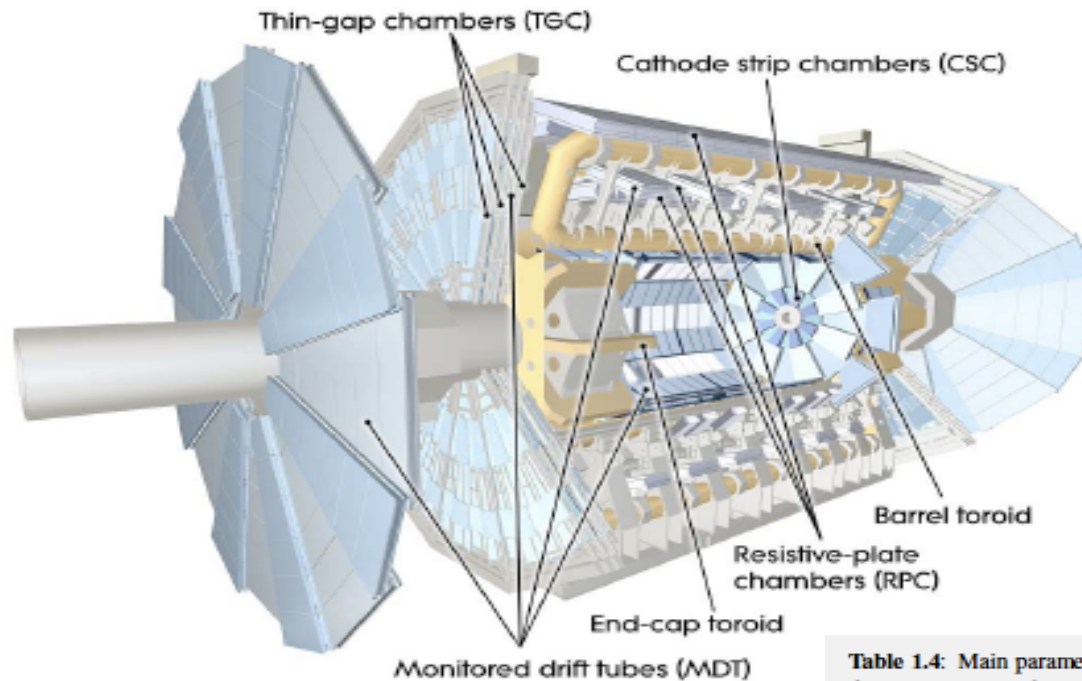**Figure 1.3**: Cut-away view of the ATLAS calorimeter system.

A view of the sampling calorimeters is presented in figure 1.3, and the pseudorapidity coverage, granularity, and segmentation in depth of the calorimeters are summarised in table 1.3 (see also chapter 5). These calorimeters cover the range $|\eta| < 4.9$, using different techniques suited to the widely varying requirements of the physics processes of interest and of the radiation environment over this large η-range. Over the η region matched to the inner detector, the fine granularity of the EM calorimeter is ideally suited for precision measurements of electrons and photons. The coarser granularity of the rest of the calorimeter is sufficient to satisfy the physics requirements for jet reconstruction and E_T^{miss} measurements.

Table 1.3: Main parameters of the calorimeter system.

	Barrel		End-cap	
EM calorimeter				
Number of layers and $\|\eta\|$ coverage				
Presampler	1	$\|\eta\| < 1.52$	1	$1.5 < \|\eta\| < 1.8$
Calorimeter	3	$\|\eta\| < 1.35$	2	$1.375 < \|\eta\| < 1.5$
	2	$1.35 < \|\eta\| < 1.475$	3	$1.5 < \|\eta\| < 2.5$
			2	$2.5 < \|\eta\| < 3.2$
Granularity $\Delta\eta \times \Delta\phi$ versus $\|\eta\|$				
Presampler	0.025×0.1	$\|\eta\| < 1.52$	0.025×0.1	$1.5 < \|\eta\| < 1.8$
Calorimeter 1st layer	$0.025/8 \times 0.1$	$\|\eta\| < 1.40$	0.050×0.1	$1.375 < \|\eta\| < 1.425$
	0.025×0.025	$1.40 < \|\eta\| < 1.475$	0.025×0.1	$1.425 < \|\eta\| < 1.5$
			$0.025/8 \times 0.1$	$1.5 < \|\eta\| < 1.8$
			$0.025/6 \times 0.1$	$1.8 < \|\eta\| < 2.0$
			$0.025/4 \times 0.1$	$2.0 < \|\eta\| < 2.4$
			0.025×0.1	$2.4 < \|\eta\| < 2.5$
			0.1×0.1	$2.5 < \|\eta\| < 3.2$
Calorimeter 2nd layer	0.025×0.025	$\|\eta\| < 1.40$	0.050×0.025	$1.375 < \|\eta\| < 1.425$
	0.075×0.025	$1.40 < \|\eta\| < 1.475$	0.025×0.025	$1.425 < \|\eta\| < 2.5$
			0.1×0.1	$2.5 < \|\eta\| < 3.2$
Calorimeter 3rd layer	0.050×0.025	$\|\eta\| < 1.35$	0.050×0.025	$1.5 < \|\eta\| < 2.5$
Number of readout channels				
Presampler	7808		1536 (both sides)	
Calorimeter	101760		62208 (both sides)	
LAr hadronic end-cap				
$\|\eta\|$ coverage			$1.5 < \|\eta\| < 3.2$	
Number of layers			4	
Granularity $\Delta\eta \times \Delta\phi$			0.1×0.1	$1.5 < \|\eta\| < 2.5$
			0.2×0.2	$2.5 < \|\eta\| < 3.2$
Readout channels			5632 (both sides)	
LAr forward calorimeter				
$\|\eta\|$ coverage			$3.1 < \|\eta\| < 4.9$	
Number of layers			3	
Granularity $\Delta x \times \Delta y$ (cm)			FCal1: 3.0×2.6	$3.15 < \|\eta\| < 4.30$
			FCal1: $\sim$ four times finer	$3.10 < \|\eta\| < 3.15,$ $4.30 < \|\eta\| < 4.83$
			FCal2: 3.3×4.2	$3.24 < \|\eta\| < 4.50$
			FCal2: $\sim$ four times finer	$3.20 < \|\eta\| < 3.24,$ $4.50 < \|\eta\| < 4.81$
			FCal3: 5.4×4.7	$3.32 < \|\eta\| < 4.60$
			FCal3: $\sim$ four times finer	$3.29 < \|\eta\| < 3.32,$ $4.60 < \|\eta\| < 4.75$
Readout channels			3524 (both sides)	
Scintillator tile calorimeter				
	Barrel		Extended barrel	
$\|\eta\|$ coverage	$\|\eta\| < 1.0$		$0.8 < \|\eta\| < 1.7$	
Number of layers	3		3	
Granularity $\Delta\eta \times \Delta\phi$	0.1×0.1		0.1×0.1	
Last layer	0.2×0.1		0.2×0.1	
Readout channels	5760		4092 (both sides)	

Thin-gap chambers (TGC)

Cathode strip chambers (CSC)

Muon Spectrometer

Barrel toroid

Resistive-plate chambers (RPC)

End-cap toroid

Monitored drift tubes (MDT)

The conceptual layout of the muon spectrometer is shown in figure 1.4 and the main parameters of the muon chambers are listed in table 1.4 (see also chapter 6). It is based on the magnetic deflection of muon tracks in the large superconducting air-core toroid magnets, instrumented with separate trigger and high-precision tracking chambers. Over the range $|\eta| < 1.4$, magnetic bending is provided by the large barrel toroid. For $1.6 < |\eta| < 2.7$, muon tracks are bent by two smaller end-cap magnets inserted into both ends of the barrel toroid. Over $1.4 < |\eta| < 1.6$, usually referred to as the transition region, magnetic deflection is provided by a combination of barrel and end-cap fields. This magnet configuration provides a field which is mostly orthogonal to the muon trajectories, while minimising the degradation of resolution due to multiple scattering. The anticipated high level of particle flux has had a major impact on the choice and design of the spectrometer instrumentation, affecting performance parameters such as rate capability, granularity, ageing properties, and radiation hardness.

Table 1.4: Main parameters of the muon spectrometer. Numbers in brackets for the MDT's and the RPC's refer to the final configuration of the detector in 2009.

| Monitored drift tubes	MDT
- Coverage	$|\eta| < 2.7$ (innermost layer: $|\eta| < 2.0$)
- Number of chambers	1088 (1150)
- Number of channels	339 000 (354 000)
- Function	Precision tracking
Cathode strip chambers	**CSC**
- Coverage	$2.0 < |\eta| < 2.7$
- Number of chambers	32
- Number of channels	31 000
- Function	Precision tracking
Resistive plate chambers	**RPC**
- Coverage	$|\eta| < 1.05$
- Number of chambers	544 (606)
- Number of channels	359 000 (373 000)
- Function	Triggering, second coordinate
Thin gap chambers	**TGC**
- Coverage	$1.05 < |\eta| < 2.7$ (2.4 for triggering)
- Number of chambers	3588
- Number of channels	318 000
- Function	Triggering, second coordinate

1.5   Forward detectors

Three smaller detector systems cover the ATLAS forward region (see chapter 7). The main function of the first two systems is to determine the luminosity delivered to ATLAS. At ± 17 m from the interaction point lies LUCID (LUminosity measurement using Cerenkov Integrating Detector). It detects inelastic $p\text{-}p$ scattering in the forward direction, and is the main online relative-luminosity monitor for ATLAS. The second detector is ALFA (Absolute Luminosity For ATLAS). Located at ± 240 m, it consists of scintillating fibre trackers located inside Roman pots which are designed to approach as close as 1 mm to the beam. The third system is the Zero-Degree Calorimeter (ZDC), which plays a key role in determining the centrality of heavy-ion collisions. It is located at ± 140 m from the interaction point, just beyond the point where the common straight-section vacuum-pipe divides back into two independent beam-pipes. The ZDC modules consist of layers of alternating quartz rods and tungsten plates which will measure neutral particles at pseudorapidities $|\eta| \geq 8.2$.
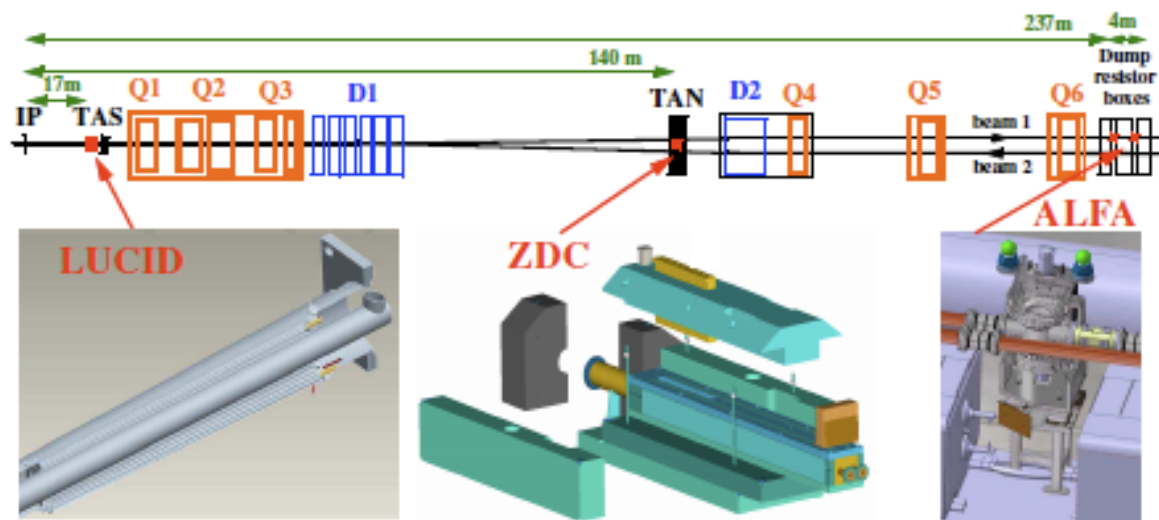
Figure 7.1: Placement of the forward detectors along the beam-line around the ATLAS interaction point (IP). See text for details.

Luminosity measurements …

CMS/TOTEM and ATLAS forward detectors for forward physics, heavy ion, … and luminosity measurements

[5.2 ≤ η ≤ 6.6]

CASTOR **TOTEM**

(z = ±140 m)

ZDC [η ≥ 8.3 neutral]
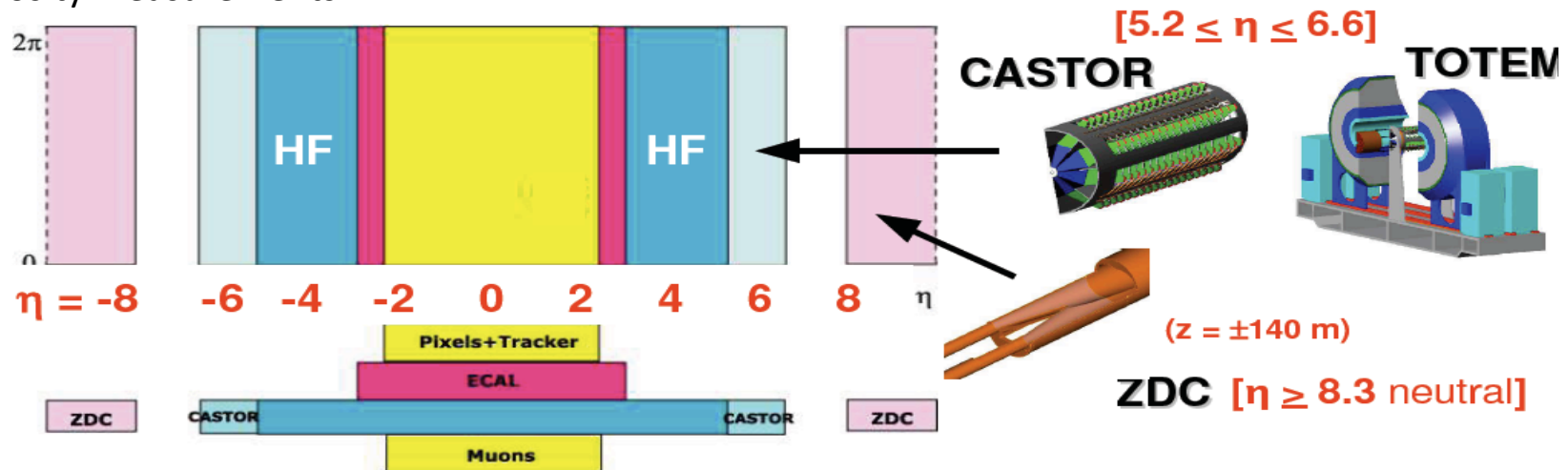
- **Initially from machine parameters**
  - Precision ~10-15%

Depends on f_{rev} revolution frequency
n_b number of bunches
N number of particles/bunch
σ* beam size or rather overlap integral at IP

$$\mathcal{L} = \frac{N^2 f_{rev} n_b}{4\pi \sigma^{*2}}$$

- **Medium term from physics processes:W/Z & μμ/ee**
  - Precision ~5-10%
- **>= 2011 from Roman Pot detectors**
  - Precision ~2-3%
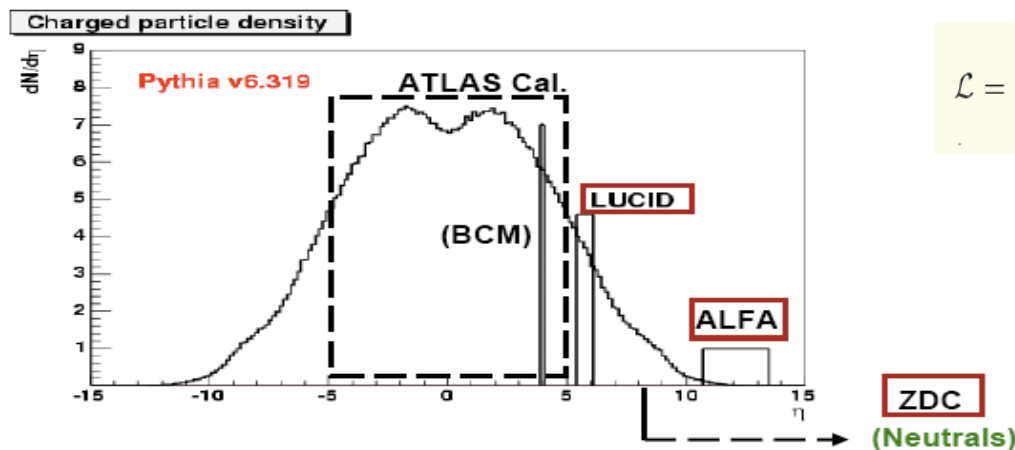
ATLAS Magnets

Figure 2.2: Bare central solenoid in the factory after completion of the coil winding.
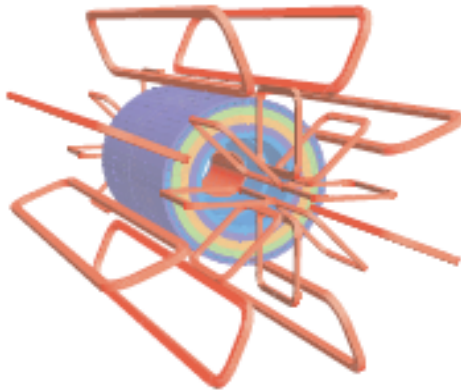
Figure 2.1: Geometry of magnet windings and tile calorimeter steel. The eight barrel toroid coils, with the end-cap coils interleaved are visible. The solenoid winding lies inside the calorimeter volume. The tile calorimeter is modelled (section 2.2.2) by four layers with different magnetic properties, plus an outside return yoke. For the sake of clarity the forward shielding disk (section 3.2) is not displayed.

Table 2.1: Main parameters of the ATLAS magnet system.

Property	Feature	Unit	Solenoid	Barrel toroid	End-cap toroids
Size	Inner diameter	m	2.46	9.4	1.65
	Outer diameter	m	2.56	20.1	10.7
	Axial length	m	5.8	25.3	5.0
	Number of coils		1	8	2 × 8
Mass	Conductor	t	3.8	118	2 × 20.5
	Cold mass	t	5.4	370	2 × 140
	Total assembly	t	5.7	830	2 x 239
Coils	Turns per coil		1154	120	116
	Nominal current	kA	7.73	20.5	20.5
	Magnet stored energy	GJ	0.04	1.08	2 x 0.25
	Peak field in the windings	T	2.6	3.9	4.1
	Field range in the bore	T	0.9–2.0	0.2–2.5	0.2–3.5
Conductor	Overall size	mm^2	30 x 4.25	57 x 12	41 x 12
	Ratio Al:Cu:NbTi		15.6:0.9:1	28:1.3:1	19:1.3:1
	Number of strands (NbTi)		12	38–40	40
	Strand diameter (NbTi)	mm	1.22	1.3	1.3
	Critical current (at 5 T and 4.2 K)	kA	20.4	58	60
	Operating/critical-current ratio at 4.5 K	%	20	30	30
	Residual resistivity ratio (RRR) for Al		> 500	> 800	> 800
	Temperature margin	K	2.7	1.9	1.9
	Number of units × length	m	4 × 2290	8 × 4 × 1730	2 × 8 × 2 × 800
	Total length (produced)	km	10	56	2 x 13
Heat load	At 4.5 K	W	130	990	330
	At 60–80 K	kW	0.5	7.4	1.7
	Liquid helium mass flow	g/s	7	410	280
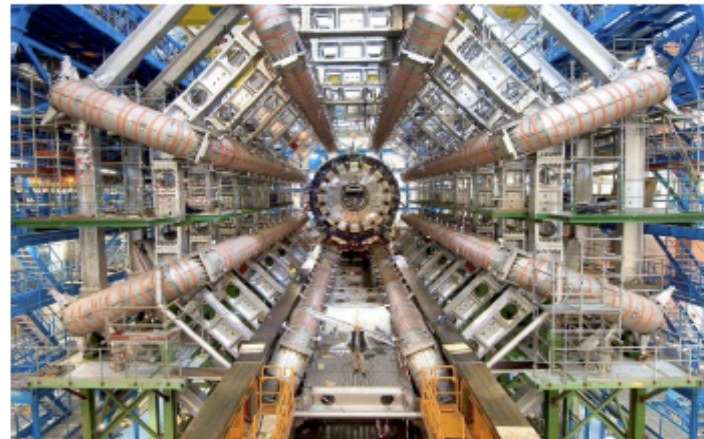
Figure 2.3: Barrel toroid as installed in the underground cavern; note the symmetry of the supporting structure. The temporary scaffolding and green platforms were removed once the installation was complete. The scale is indicated by the person standing in between the two bottom coils. Also visible are the stainless-steel rails carrying the barrel calorimeter with its embedded solenoid, which await translation towards their final position in the centre of the detector.

Cross section and rate at the LHC
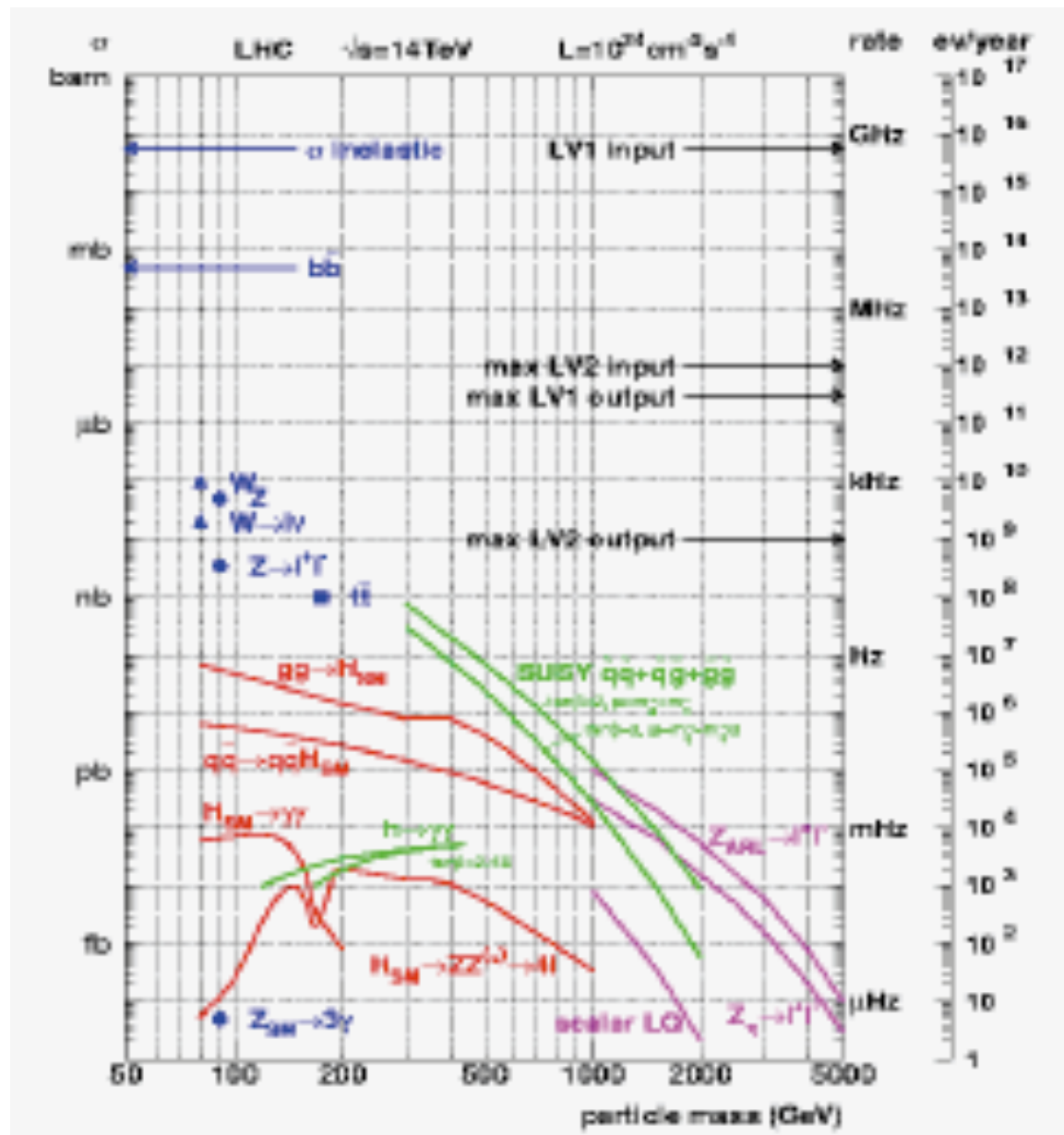
## 1.6 Trigger, readout, data acquisition, and control systems

The Trigger and Data Acquisition (collectively TDAQ) systems, the timing- and trigger-control logic, and the Detector Control System (DCS) are partitioned into sub-systems, typically associated with sub-detectors, which have the same logical components and building blocks (see chapter 8).

The trigger system has three distinct levels: L1, L2, and the event filter. Each trigger level refines the decisions made at the previous level and, where necessary, applies additional selection criteria. The data acquisition system receives and buffers the event data from the detector-specific readout electronics, at the L1 trigger accept rate, over 1600 point-to-point readout links. The first level uses a limited amount of the total detector information to make a decision in less than 2.5 μs, reducing the rate to about 75 kHz. The two higher levels access more detector information for a final rate of up to 200 Hz with an event size of approximately 1.3 Mbyte.
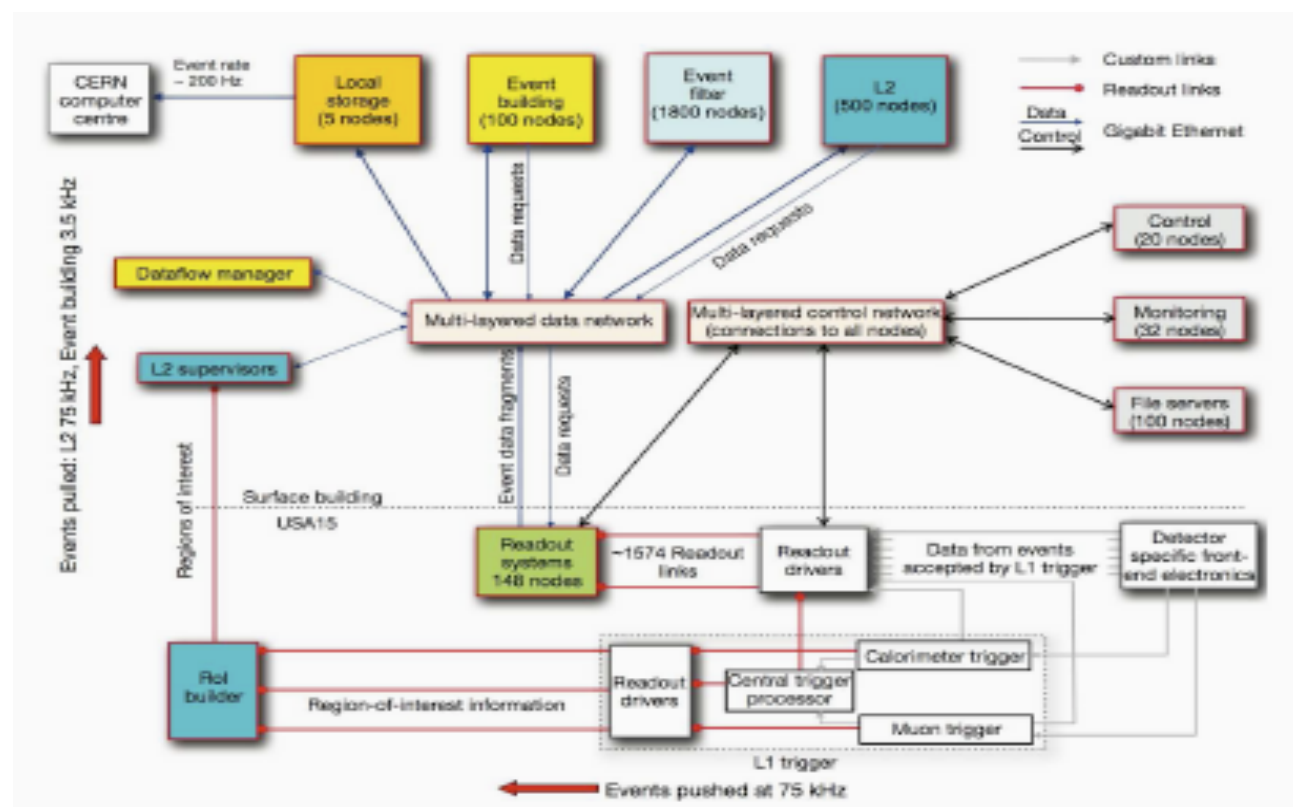
Level 1 Trigger
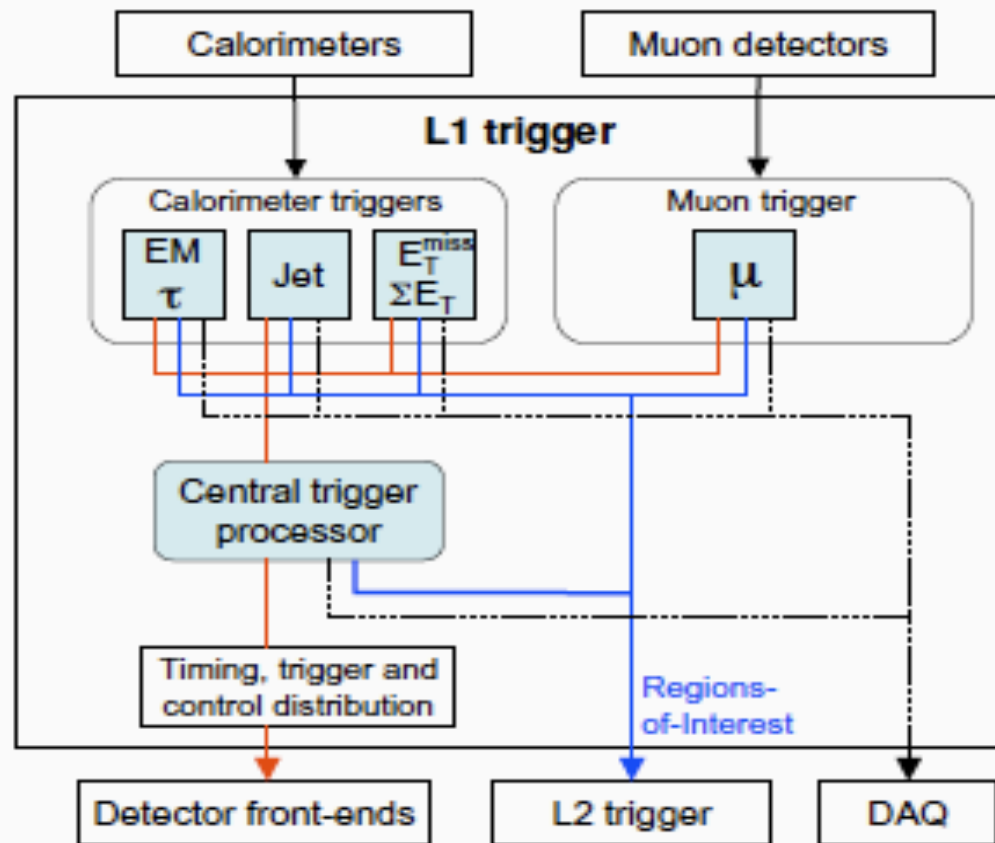
Figure 8.2: Block diagram of the L1 trigger. The overall L1 accept decision is made by the central trigger processor, taking input from calorimeter and muon trigger results. The paths to the detector front-ends, L2 trigger, and data acquisition system are shown from left to right in red, blue and black, respectively.

Alignment
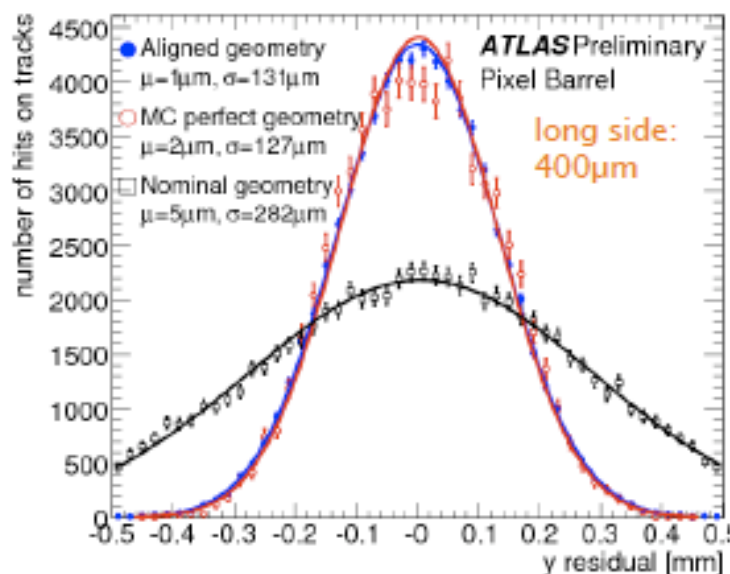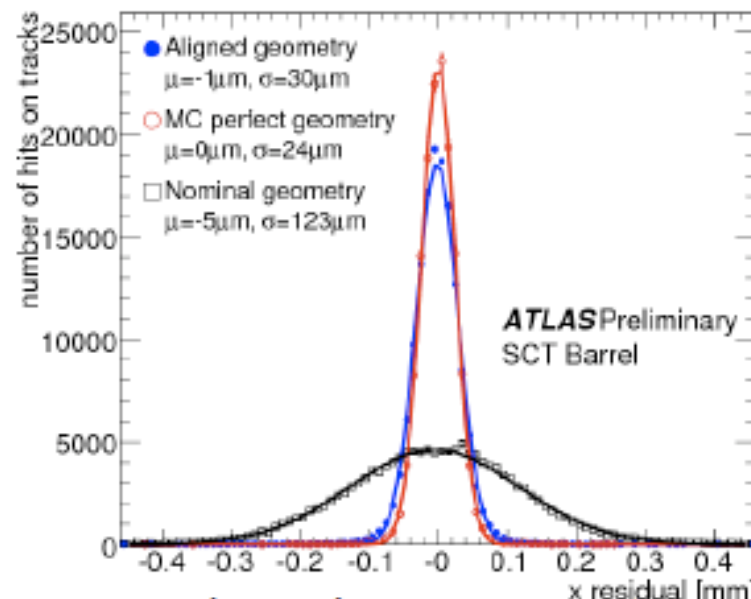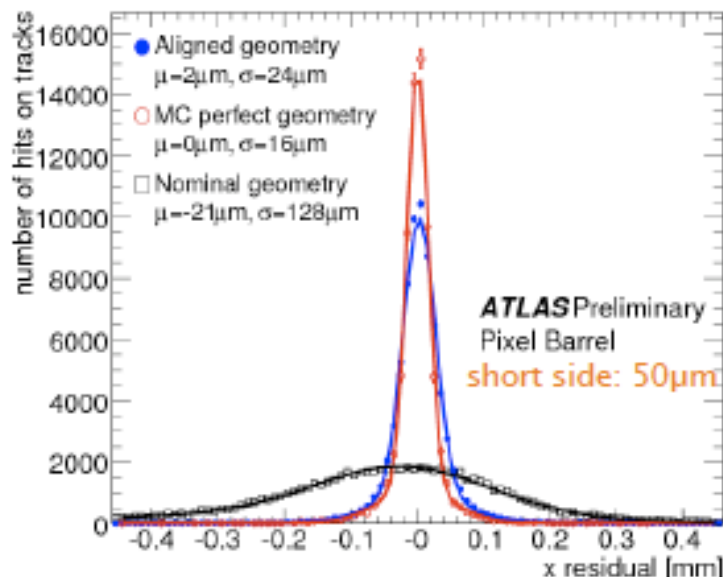
→ Si detectors aligned at ≤ 20 μm (2008)
→ stable in 2009

Laurent Vacavant
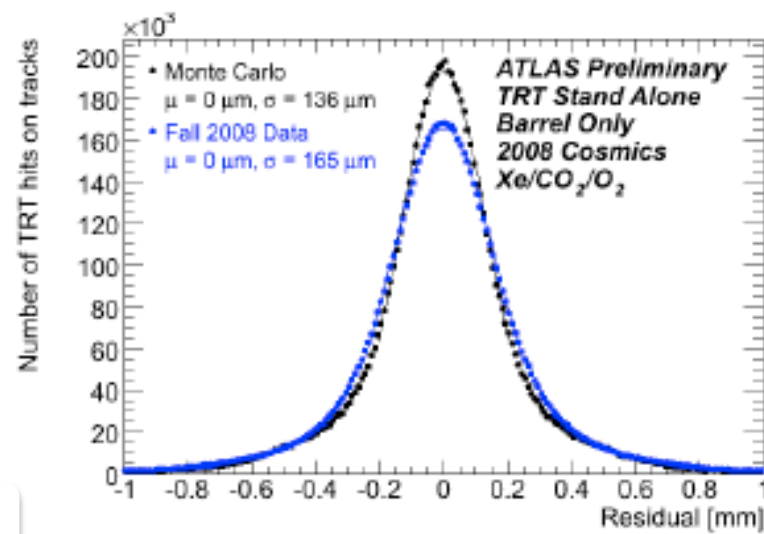
Materials in the front of the ATLAS calorimeter
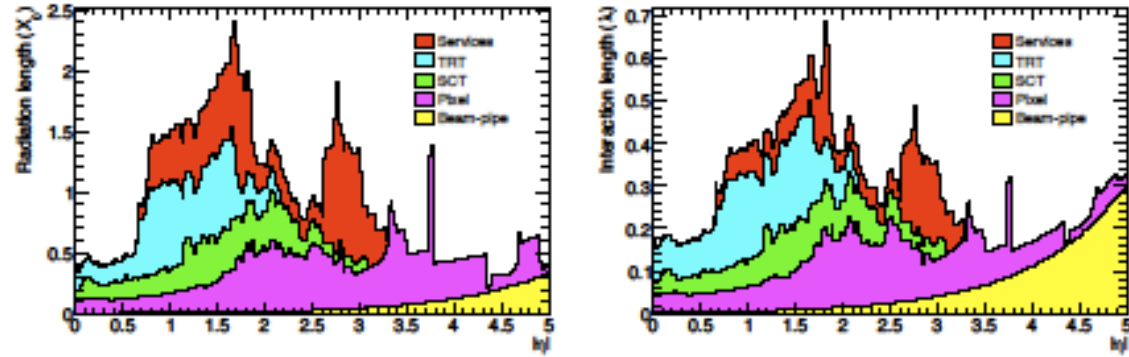
Figure 4.45: Material distribution (X_0, λ) at the exit of the ID envelope, including the services and thermal enclosures. The distribution is shown as a function of $|\eta|$ and averaged over ϕ. The breakdown indicates the contributions of external services and of individual sub-detectors, including services in their active volume.
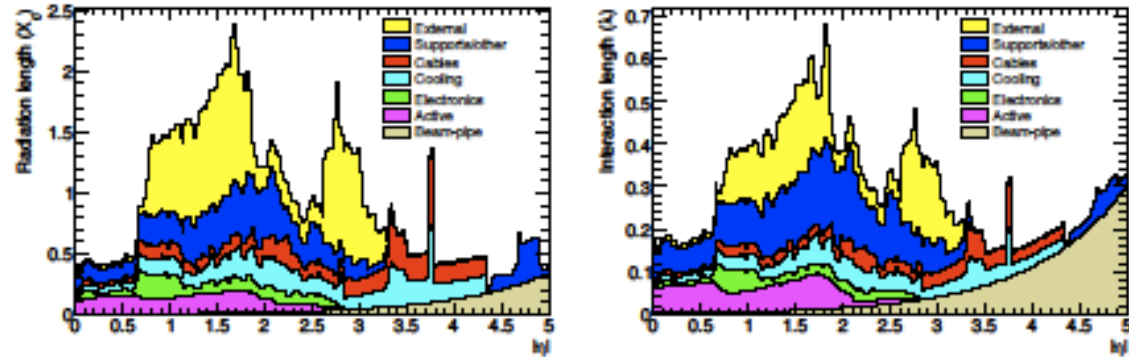
Figure 4.46: Material distribution (X_0, λ) at the exit of the ID envelope, including the services and thermal enclosures. The distribution is shown as a function of $|\eta|$ and averaged over ϕ. The breakdown shows the contributions of different ID components, independent of the sub-detector.
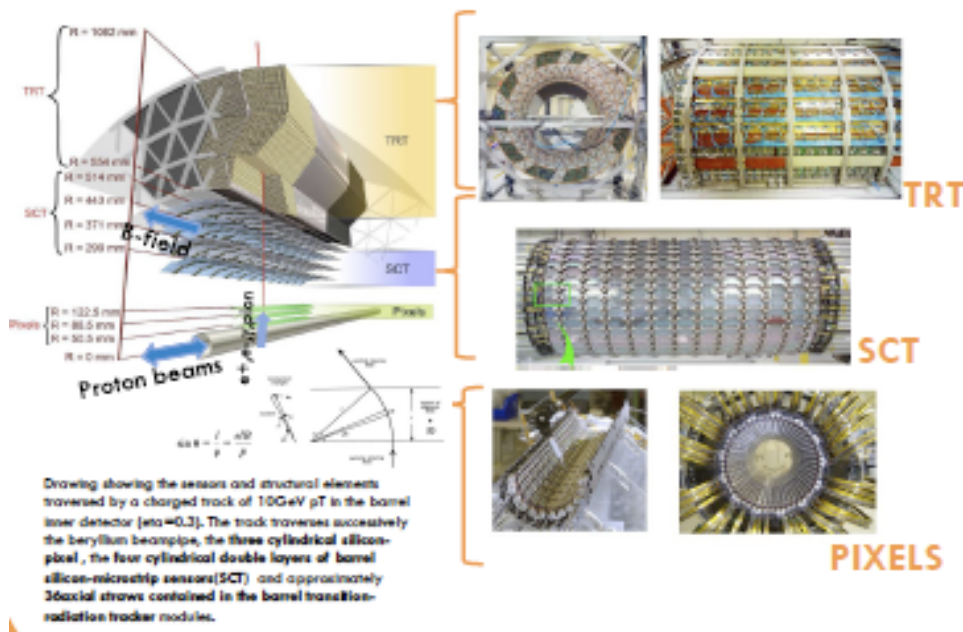
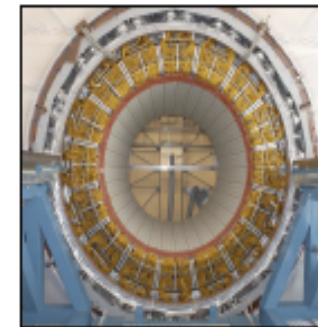# Materials in the front of the ATLAS calorimeter
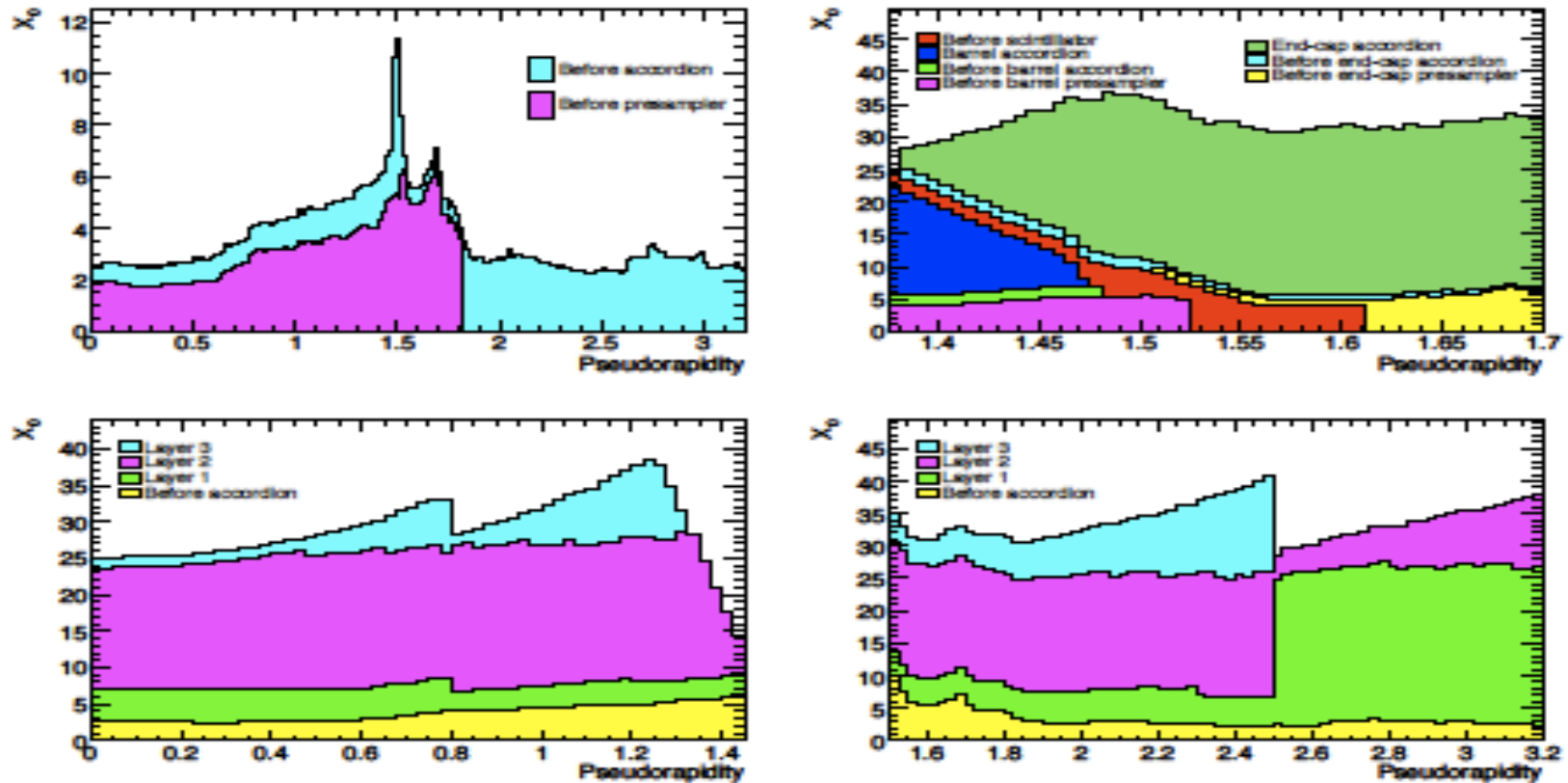
Figure 5.1: Cumulative amounts of material, in units of radiation length X_0 and as a function of $|\eta|$, in front of and in the electromagnetic calorimeters. The top left-hand plot shows separately the total amount of material in front of the presampler layer and in front of the accordion itself over the full η-coverage. The top right-hand plot shows the details of the crack region between the barrel and end-cap cryostats, both in terms of material in front of the active layers (including the crack scintillator) and of the total thickness of the active calorimeter. The two bottom figures show, in contrast, separately for the barrel (left) and end-cap (right), the thicknesses of each accordion layer as well as the amount of material in front of the accordion.

Materials in the front of the ATLAS calorimeter
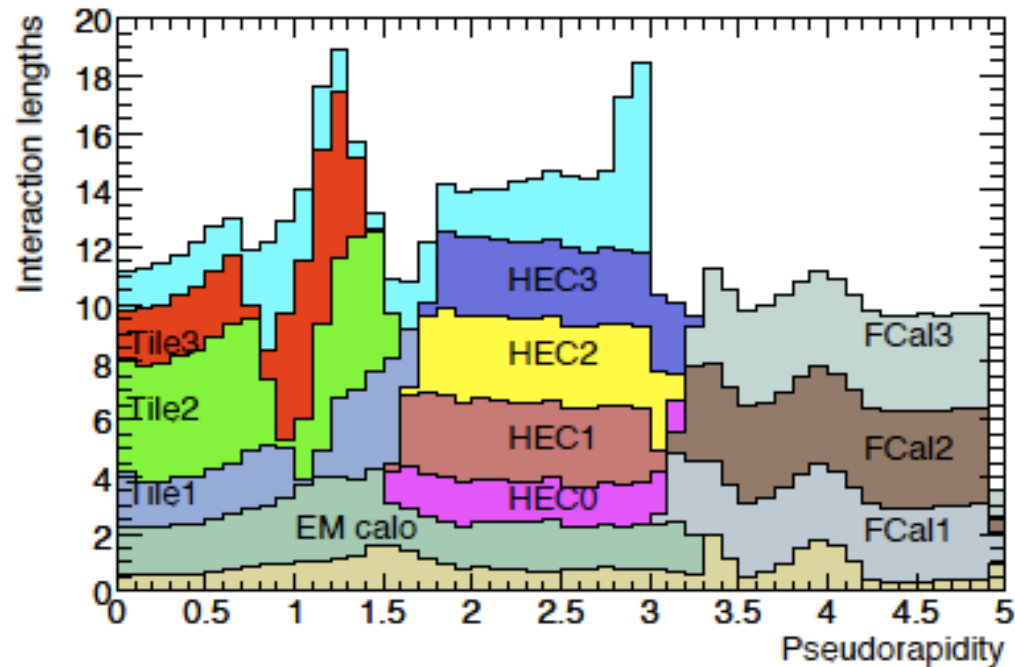
Figure 5.2: Cumulative amount of material, in units of interaction length, as a function of $|\eta|$, in front of the electromagnetic calorimeters, in the electromagnetic calorimeters themselves, in each hadronic layer, and the total amount at the end of the active calorimetry. Also shown for completeness is the total amount of material in front of the first active layer of the muon spectrometer (up to $|\eta| < 3.0$).
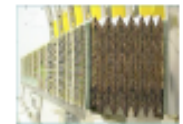
Electron identification: Track/Cluster matching

Drawing showing the sensors and structural elements traversed by a charged track of 10GeV pT in the barrel inner detector (eta =0.3). The track traverses successively the beryllium beampipe, the three cylindrical silicon-pixel, the four cylindrical double layers of barrel silicon-microstrip sensors(SCT) and approximately 36 axial straws contained in the barrel transition-radiation tracker modules.

TRT

SCT

PIXELS

Electron = track in the Inner Detector (direction measurement) Matched to an EM cluster in the calorimeter (energy measurement). Need to know:
 - material distribution in the Inner detector in the front of the EM calorimeter
  - calibration of the energy response of the calorimeter
  - rejection against jet faking electrons

The EM calorimeter half barrel and cryostat   calorimeter module

calorimeter module in cryostat (testbeam)

Layers and granularity ($\Delta\eta \times \Delta\phi$) in barrel:
Presampler (0.025 x 0.1)
Strips (0.003 x 0.1)
Middle (0.025 x 0.025)
Back (0.05 x 0.025)

one cell
In the middle
Layer
(0.025x0.025)
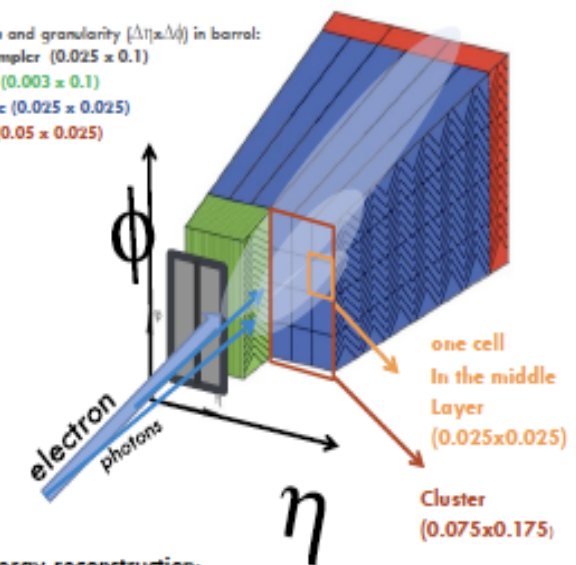
Cluster
(0.075x0.175)

LAr energy reconstruction:

Cell energy: $E(GeV) = f_{DAC \to \mu A} \times f_{\mu A \to GeV} \times \frac{M_{cali}}{M_{phys}} \times g_{ADC \to DAC} \sum_{i=1}^{n} a_i(S_i - P)$

Electronic calibration constants:
p = pedestal
a = optimal filtering
f,g = ADC → GeV
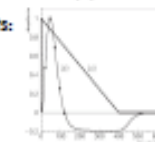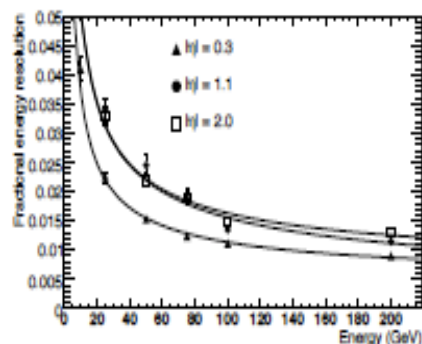
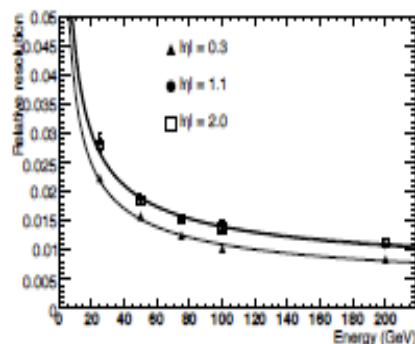Cluster: sum of cell energies over all layers

Electron identification

Figure 10.46: Difference between measured and true energy normalised to true energy for electrons with an energy of 100 GeV at $\eta = 0.325$.
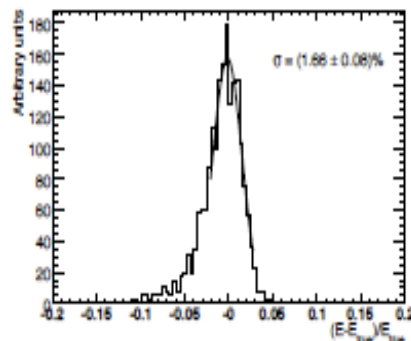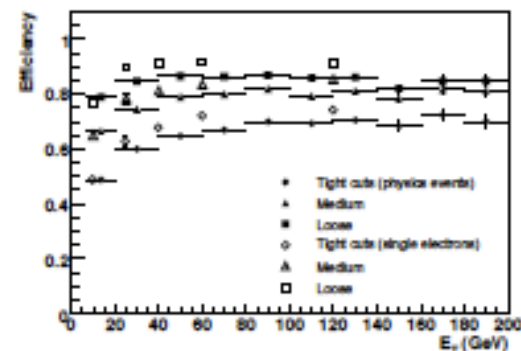

Figure 10.47: Difference between measured and true energy normalised to true energy for electrons with an energy of 100 GeV at $\eta = 1.075$.
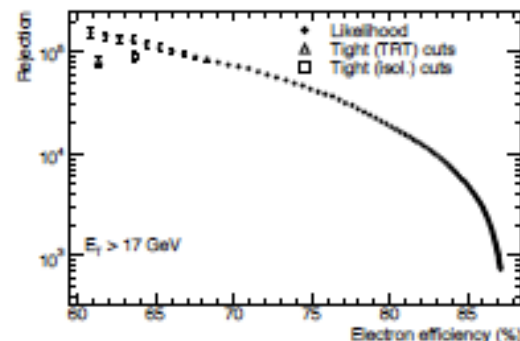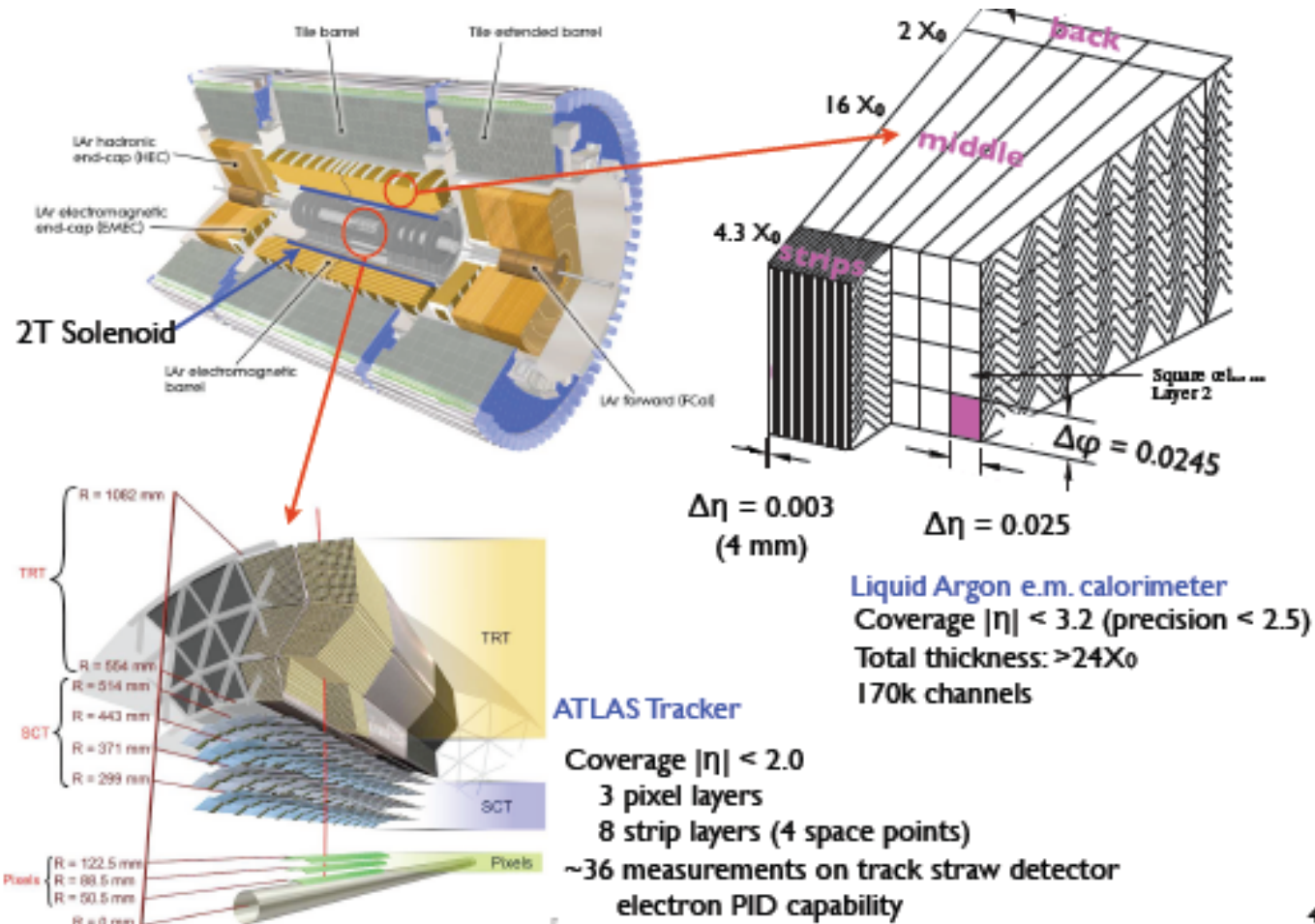

Figure 10.56: Overall reconstruction and identification efficiency of various levels of electron cuts: loose, medium, and tight isol. as a function of E_T for single electrons (open symbols) and for isolated electrons in a sample of physics events with a busy environment (full symbols).

Figure 10.50: Expected relative energy resolution as a function of energy for electrons at $|\eta| = 0.3$, 1.1, and 2.0. The curves represent fits to the points at the same $|\eta|$ by a function containing a stochastic term, a constant term and a noise term.

Figure 10.51: Expected relative energy resolution as a function of energy for photons at $|\eta| = 0.3$, 1.1, and 2.0. The curves represent fits to the points at the same η by a function containing a stochastic term, a constant term and a noise term.

Figure 10.57: Jet rejection as a function of overall reconstruction and identification efficiency for electrons, as obtained using a likelihood method (full circles). The results obtained with the standard cut-based method are also shown in the case of tight TRT (open triangle) and tight isol. (open square) cuts.

27

Photon identification

Tile barrel Tile extended barrel

2 X₀ back

16 X₀ middle

LAr hadronic end-cap (HEC)

4.3 X₀ strips

LAr electromagnetic end-cap (EMEC)

2T Solenoid

LAr electromagnetic barrel

LAr forward (FCal)

Square cells ... Layer 2

$\Delta\varphi = 0.0245$

$\Delta\eta = 0.003$ (4 mm)

$\Delta\eta = 0.025$

Liquid Argon e.m. calorimeter
Coverage $|\eta| < 3.2$ (precision < 2.5)
Total thickness: $>24X_0$
170k channels

TRT

R = 1082 mm
R = 554 mm
R = 514 mm
R = 443 mm
R = 371 mm
R = 299 mm
R = 122.5 mm
R = 88.5 mm
R = 50.5 mm
R = 0 mm

SCT

TRT

Pixels

ATLAS Tracker
Coverage $|\eta| < 2.0$
  3 pixel layers
  8 strip layers (4 space points)
  ~36 measurements on track straw detector
    electron PID capability

Photon = no track in the Inner Detector and an EM cluster in the calorimeter
However: because of materials in the Inner Detector and in front of the calorimeter,
Photon may convert into e-e+ pair. → photon may be reconstructed as single or double
Track conversion

Photon identification
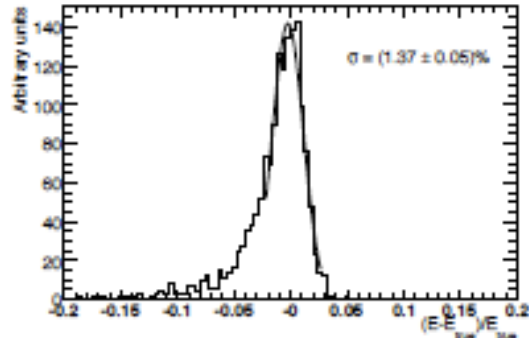
Figure 10.48: Difference between measured and true energy normalised to true energy for all photons with an energy of 100 GeV at $\eta = 1.075$.
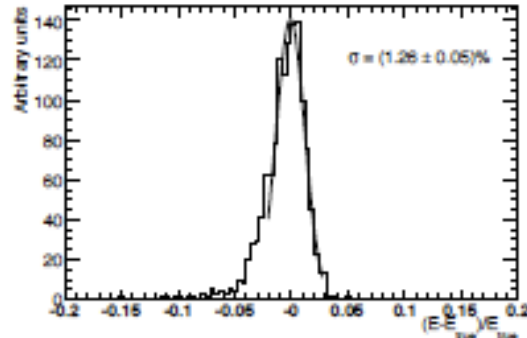

Figure 10.49: Difference between measured and true energy normalised to true energy for unconverted photons with an energy of 100 GeV at $\eta = 1.075$.
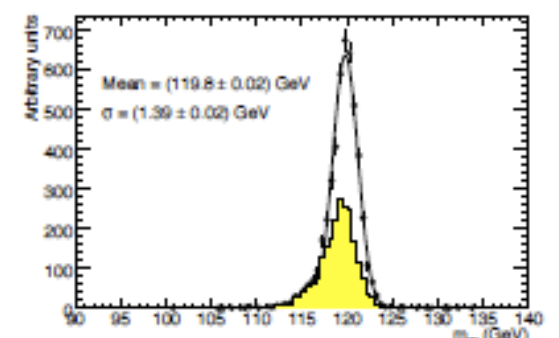
Figure 10.61: Expected distribution for the invariant mass of the two photons from Higgs-boson decays with $m_H = 120$ GeV. The shaded plot corresponds to events in which at least one of the two photons converted at a radius below 80 cm.
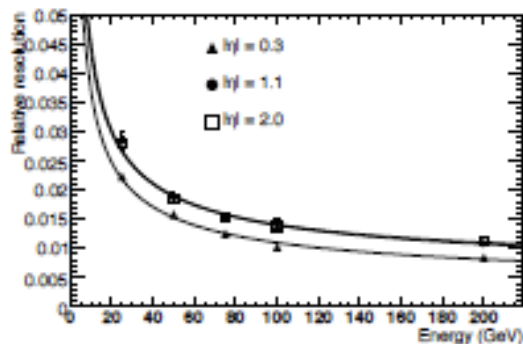
Figure 10.51: Expected relative energy resolution as a function of energy for photons at $|\eta| = 0.3$, 1.1, and 2.0. The curves represent fits to the points at the same η by a function containing a stochastic term, a constant term and a noise term.
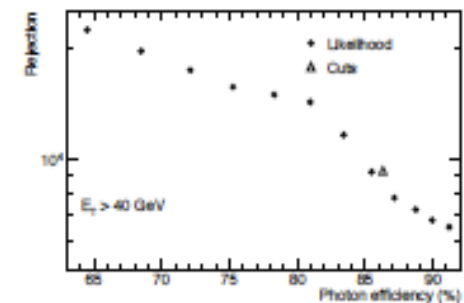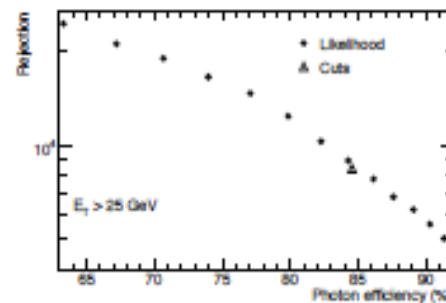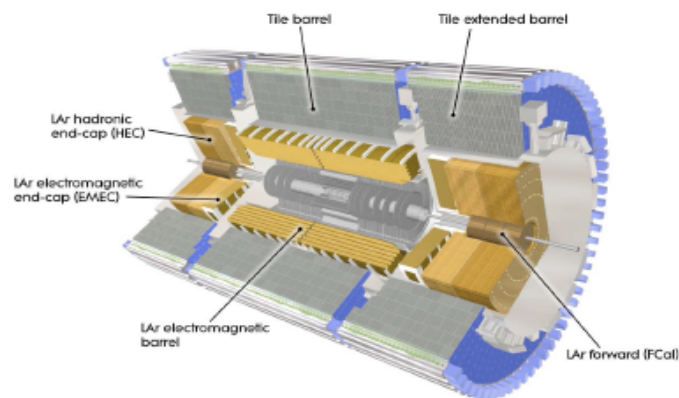

Figure 10.59: For reconstructed photon candidates with $E_T > 25$ GeV (left) and with $E_T > 40$ GeV (right), jet rejection as a function of photon efficiency, as obtained using a likelihood method. The results obtained with the standard cut-based method are also shown for reference.
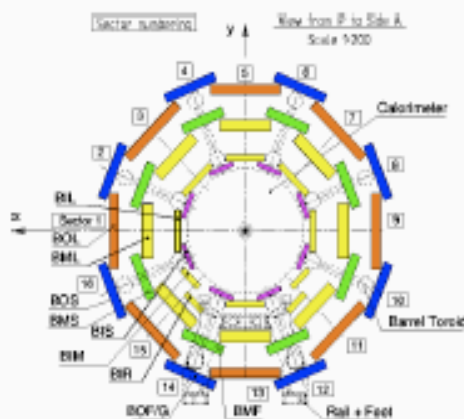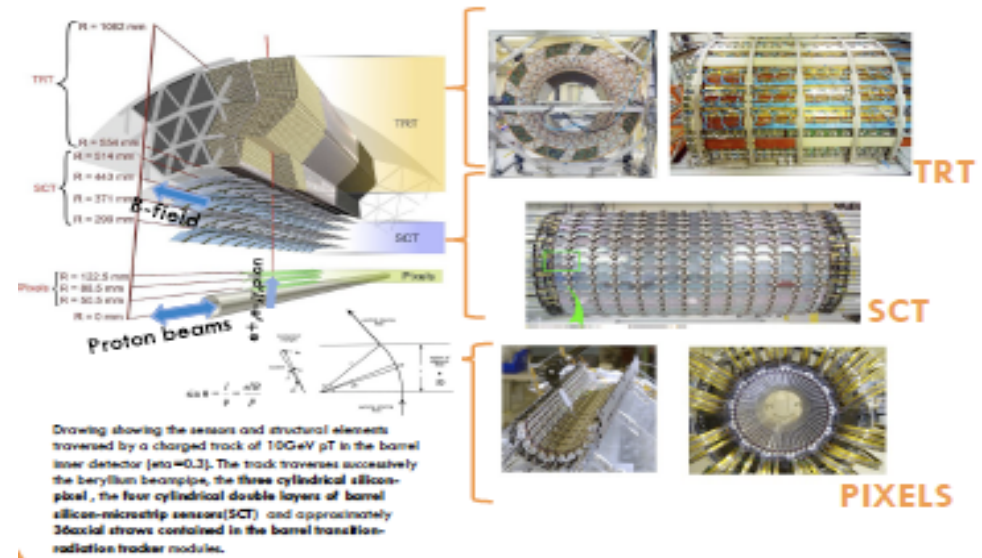
Muon identification

Muon: identified as tracks in the
Inner Detector and the Muon Spectrometer.
For muon with enough energy to pass
through the calorimeter, then energy loss
in the calorimeter must be corrected for.

Internal alignment of Muon chambers
important and relative alignment of the
inner Detector and Muon Spectrometer
also important to match track segments
From both detectors.

Magnetic field mapping also
important

Drawing showing the sensors and structural elements traversed by a charged track of 10GeV pT in the barrel inner detector (eta =0.3). The track traverses successively the beryllium beampipe, the three cylindrical silicon-pixel, the four cylindrical double layers of barrel silicon-microstrip sensors(SCT) and approximately 36 axial straws contained in the barrel transition-radiation tracker modules.

TRT

SCT

PIXELS

Figure 1.3: Cut-away view of the ATLAS calorimeter system.

Figure 6.1: Cross-section of the barrel muon system perpendicular to the beam axis (non-bending plane), showing three concentric cylindrical layers of eight large and eight small chambers. The outer diameter is about 20 m.
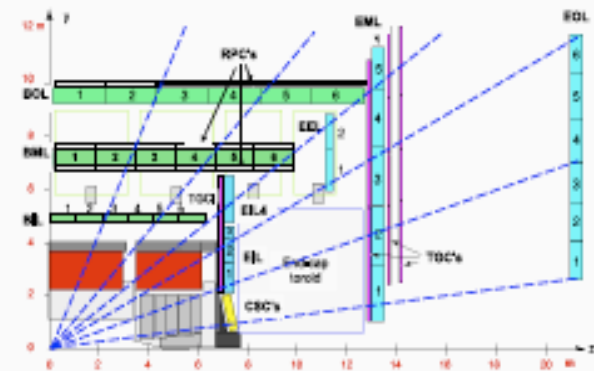
Figure 6.2: Cross-section of the muon system in a plane containing the beam axis (bending plane). Infinite-momentum muons would propagate along straight trajectories which are illustrated by the dashed lines and typically traverse three muon stations.
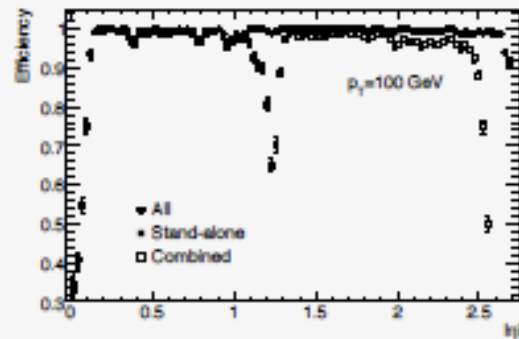
Muon Identification
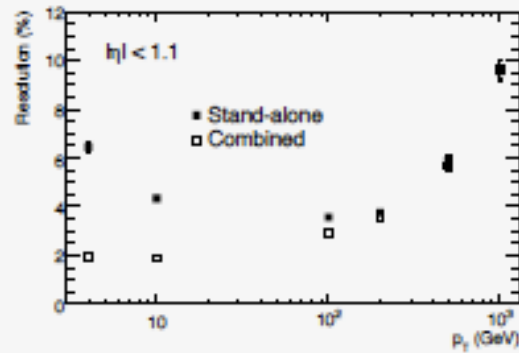
Figure 10.35: Expected stand-alone and combined fractional momentum resolution as a function of p_T for single muons with $|\eta| < 1.1$.
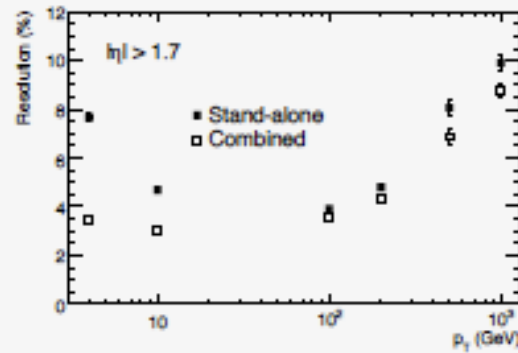
Figure 10.36: Expected stand-alone and combined fractional momentum resolution as a function of p_T for single muons with $|\eta| > 1.7$.

Figure 10.37: Efficiency for reconstructing muons with $p_T = 100\,\text{GeV}$ as a function of $|\eta|$. The results are shown for stand-alone reconstruction, combined reconstruction and for the combination of these with the segment tags discussed in the text.
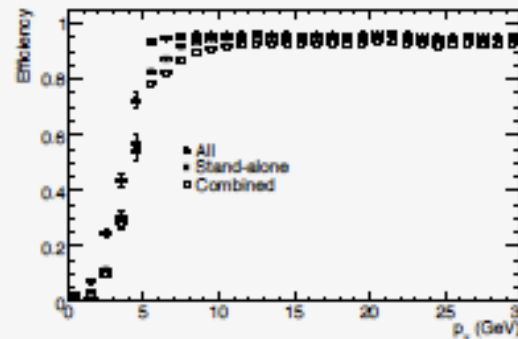
Figure 10.38: Efficiency for reconstructing muons as a function of p_T. The results are shown for stand-alone reconstruction, combined reconstruction and for the combination of these with the segment tags discussed in the text.
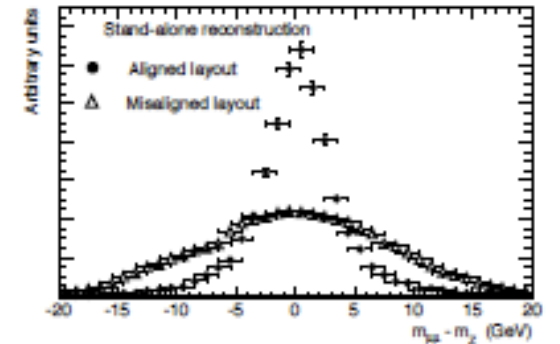
Figure 10.39: For stand-alone muon reconstruction, reconstructed invariant mass distribution of dimuons from $Z \rightarrow \mu\mu$ decays for an aligned layout of the chambers and for a misaligned layout, where all chambers are displaced and rotated randomly by typically 1 mm and 1 mrad.
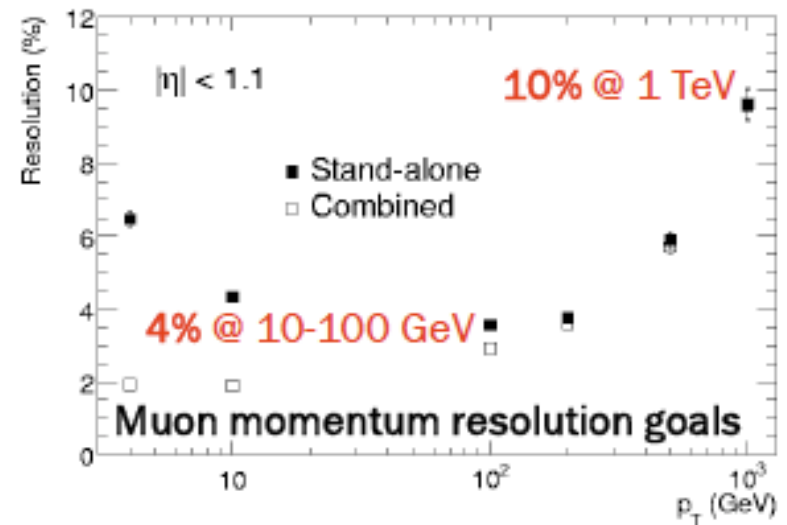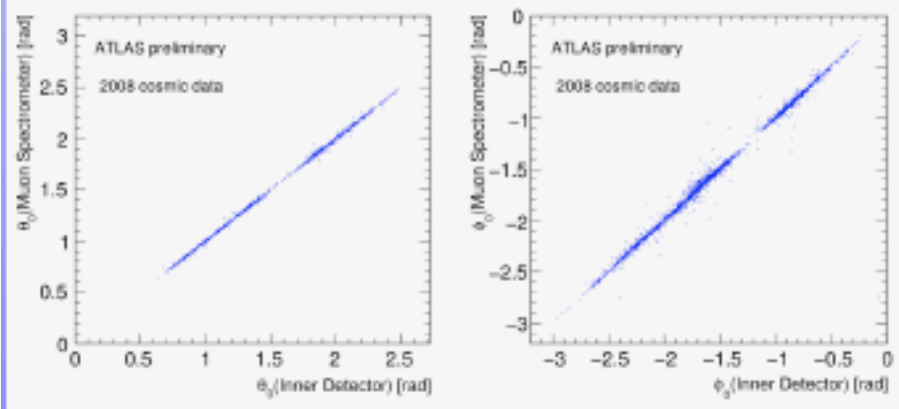
Muon Identification
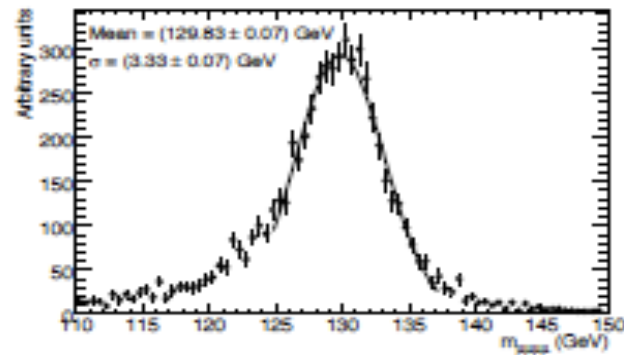
Figure 10.40: For $H \rightarrow \mu\mu\mu\mu$ decays with $m_H = 130\,\mathrm{GeV}$, reconstructed mass of the four muons using stand-alone reconstruction. The results do not include a Z-mass constraint.
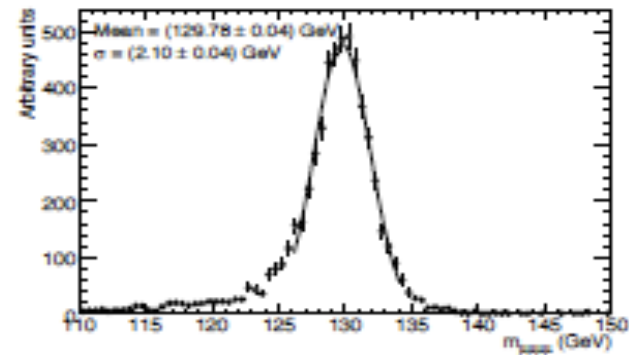
Figure 10.41: For $H \rightarrow \mu\mu\mu\mu$ decays with $m_H = 130\,\mathrm{GeV}$, reconstructed mass of the four muons using combined reconstruction. The results do not include a Z-mass constraint.

Correlation between Muon Spectrometer and Inner Detector track parameters

$|\eta| < 1.1$

10% @ 1 TeV

■ Stand-alone
□ Combined

4% @ 10-100 GeV

**Muon momentum resolution goals**

32

Hadronic tau identification

The transverse momentum range of interest spans from below 10 GeV up to 500 GeV. τ leptons decay hadronically in 64.8% of all cases, while in $\sim$ 17.8% (17.4%) of the cases they decay to an electron (muon) [1]. From the detection point of view, hadronic modes are divided by the number of charged πs among the decay products into single-prong (one charged π) and three-prong (three charged πs) decays. The small fraction (0.1%) of five-prong decays is usually too hard to detect in a jet environment. The $\tau \to \pi^{\pm} \nu$ mode contributes 22.4% to single-prong hadronic decays and the $\tau \to n\pi^0 \pi^{\pm} \nu$ modes 73.5%. For three-prong decays, the $\tau \to 3\pi^{\pm} \nu$ decay contributes 61.6%, and the $\tau \to n\pi^0 3\pi^{\pm} \nu$ mode only 33.7%. In general, one- and three-prong modes are dominated by final states consisting of $\pi^{\pm}$ and π^0.

Properties of hadronically decaying τ-leptons:
- Collimated energy deposition in calorimeter
- 1 or 3 charged decay products ($\pi^{\pm}$)
- Isolated EM clusters corresponding to π^0 in τ-decay
- Modest but significant proper lifetime
- BR ($\tau \to$ hadrons) = 64.8%
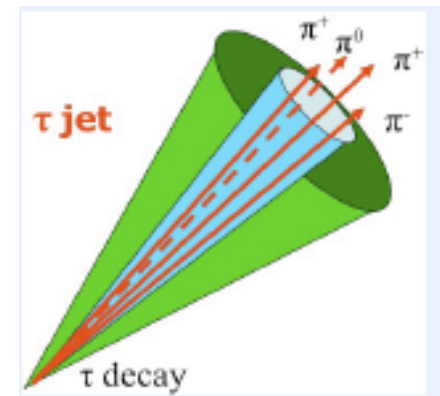
Thus also needs the tracks (Inner Detector) associated to a narrow Cluster. Need a strong rejection against jets, electrons, while maintaining high tau-jet reconstruction efficiency
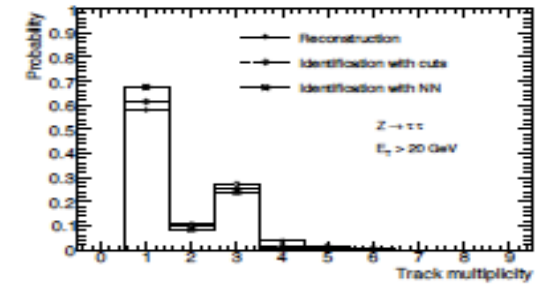
Hadronic tau identification
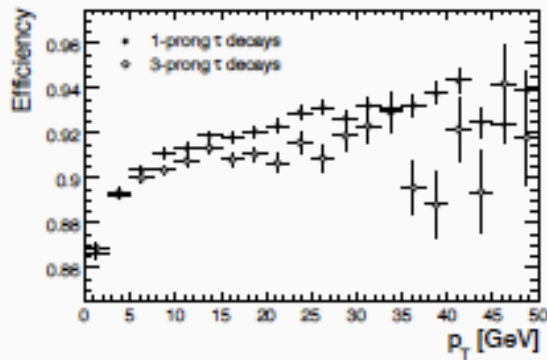
Figure 10.89: Reconstruction efficiency for charged-pion tracks as a function of the pion transverse momentum for single- and three-prong hadronic τ-decays from $W \to \tau\nu$ and $Z \to \tau\tau$ signal samples.
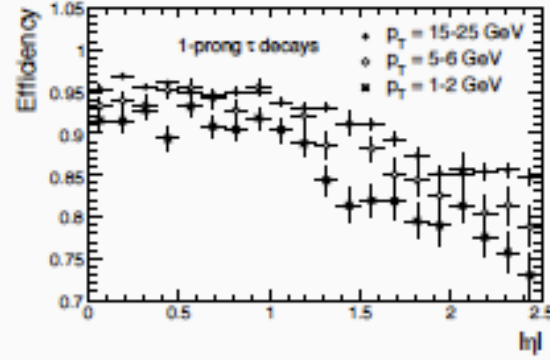

Figure 10.90: Reconstruction efficiency for the charged-pion track as a function of $|\eta|$ for three different ranges of pion p_T, for single-prong hadronic τ-decays from $W \to \tau\nu$ and $Z \to \tau\tau$ signal samples.
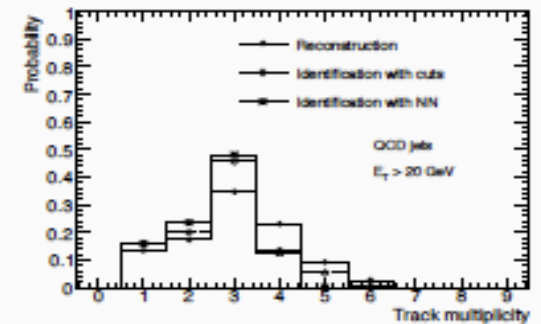

Figure 10.95: Track multiplicity distributions obtained for hadronic τ-decays with visible transverse energy above 20 GeV using the track-based τ-identification algorithm. The distributions are shown after reconstruction, after cut-based identification and finally after applying the neural network (NN) discrimination technique for an efficiency of 30% for the signal.
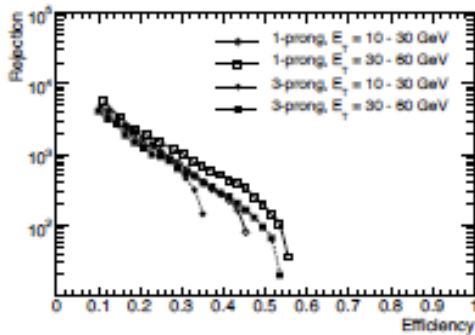
Figure 10.93: Expected rejection against hadronic jets as a function of the efficiency for hadronic τ- decays for the track-based algorithm using a neural-network selection. The results are shown separately for single- and three-prong decays and for two ranges of visible transverse energy.
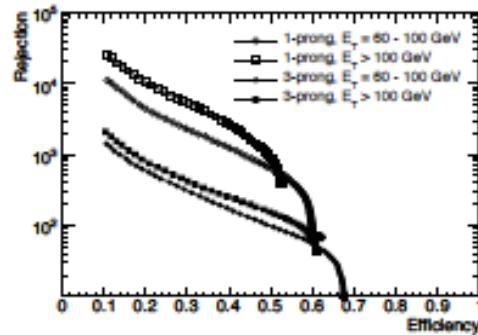
Figure 10.94: Expected rejection against hadronic jets as a function of the efficiency for hadronic τ- decays for the calorimeter-based algorithm using a likelihood selection. The results are shown separately for single- and three-prong decays and for two ranges of visible transverse energy.
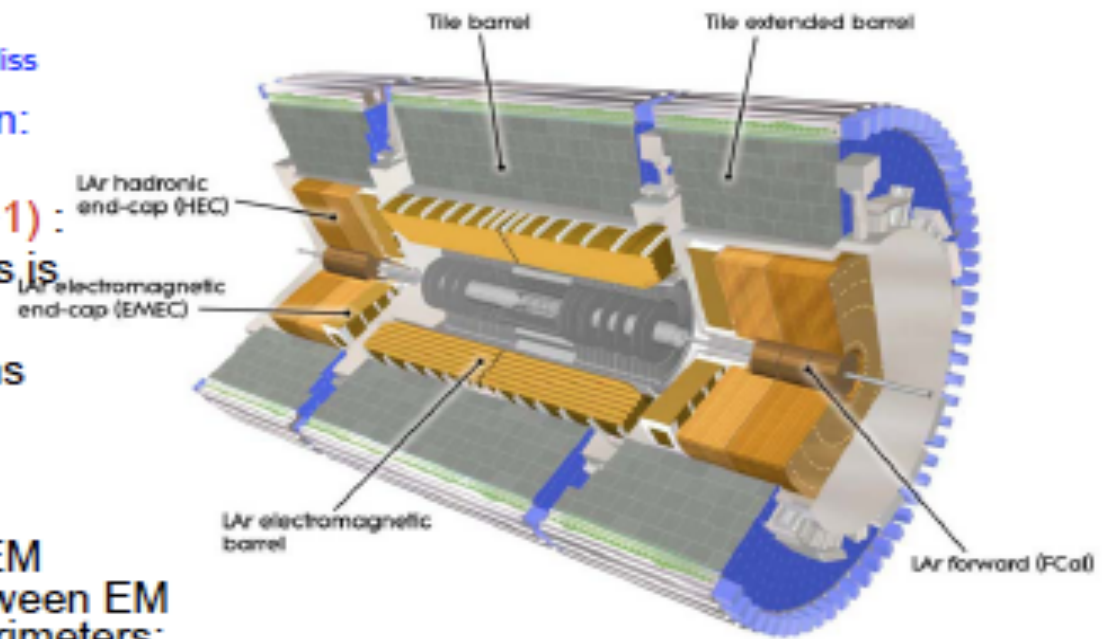

Figure 10.96: Track multiplicity distributions obtained for the background from QCD jets with visible transverse energy above 20 GeV using the track-based τ-identification algorithm. The distributions are shown after reconstruction, after cut-based identification and finally after applying the neural network (NN) discrimination technique for an efficiency of 30% for the signal.

Jet and Missing ET identification

ATLAS calorimeters

Main features for jet and E_T^{Miss} reconstruction and calibration:

- Non compensating (e/h >1):
  - Response to hadrons is lower than that to electrons and photons
  - Developed specific calibrations
- Dead material:
  - Energy loss before EM calorimeter and between EM and HAD barrel calorimeters:
    - dead material corrections
- Different technologies and many transition regions:
  - "Crack" regions: $\eta \approx 1.4, 3.2$
- Magnetic field bending

Tile barrel

Tile extended barrel

LAr hadronic end-cap (HEC)

LAr electromagnetic end-cap (EMEC)

LAr electromagnetic barrel

LAr forward (FCal)
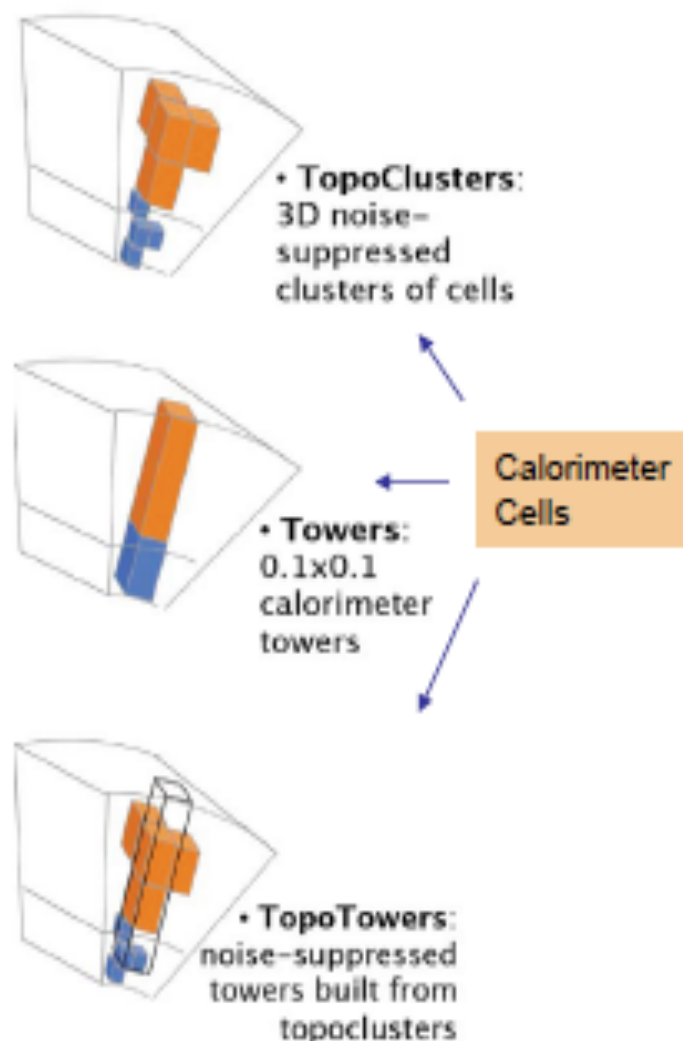
ATLAS Fiducial Regions

- Hadronic Calorimeter:
  - Barrel: $|\eta| < 1.7$
  - Endcap: $1.5 < |\eta| < 3.2$
- Electromagnetic Calorimeters
  - Barrel: $|\eta| < 1.4$
  - Endcap: $1.375 < |\eta| < 3.2$
- Forward: $3.2 < |\eta| < 4.9$

3

$\eta = -\log(\tan(\theta/2))$

Jet and Missing ET identification

- Topo-Clusters: group of calorimeter cells topologically connected
  - Noise suppression via noise-driven clustering thresholds:
    - Seed, Neighbour, Perimeter cells $(S,N,P) = (4,2,0)$
      - seed cells with $|E_{cell}| > S\sigma_{noise}$ $(S = 4)$
      - expand in 3D; add neighbours with $|E_{cell}| > N\sigma_{noise}$ $(N = 2)$
        - » merge clusters with common neighbours $(N < S)$
      - add perimeter cells with $|E_{cell}| > P\sigma_{noise}$ $(P = 0)$
  - Attempt to reconstruct single particles in calorimeter
- Towers: thin radial slice of calorimeters of fixed size

- Topo-Tower: selecting only the cells in the tower with a significant signal

- TopoClusters: 3D noise-suppressed clusters of cells

Calorimeter Cells

- Towers: 0.1x0.1 calorimeter towers

- TopoTowers: noise-suppressed towers built from topoclusters

Jet Reconstruction

Sequential process:

- Input signal selection:
    - TopoClusters, Towers, TopoTowers
- Jet finding:
    - The jet finding algorithm groups the collection of clusters(towers) according to geometrical and/or kinematic criteria.
    - Many algorithms studied in ATLAS: ⇒ recently concentrated on
        AntiKt algorithm
- Jet calibration:
    - depending on detector input signal definition, jet finder choices...
- Jet selection:
    - apply cuts on kinematics to select jets of interest
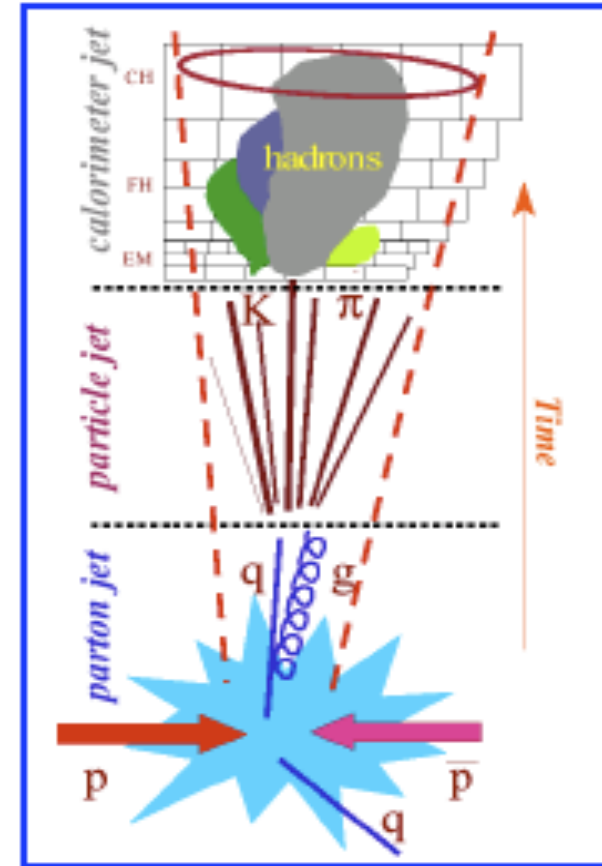
Track jets use tracks as input to the jet finding and reconstruction. This would Miss the neutral component of the jet. However track jets are useful in a Number of applications

Missing ET Reconstruction
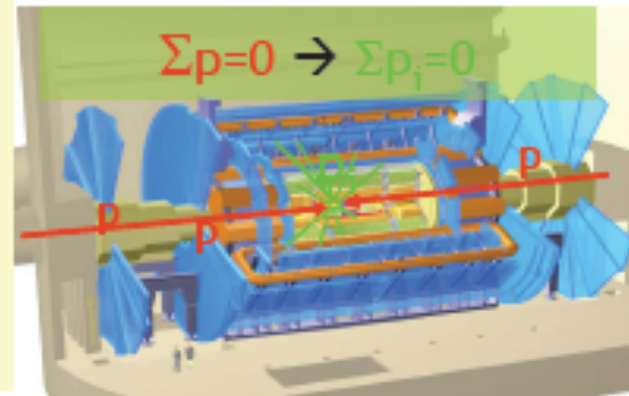
Transverse Missing Energy:

$$E_T miss = \sqrt{E_x miss^2 + E_y miss^2}$$

$$E_x miss = -\Sigma E_x$$

$$E_y miss = -\Sigma E_y$$

$$SumE_T = \Sigma E_T$$

Sum of energy of all particles seen in the detector

$\Sigma p = 0 \rightarrow \Sigma p_i = 0$

E_T^{miss} **is a complex event quantity:**

- It is calculated adding all significant signals from all detectors:
  - Calorimeter input signals (Cells, TopoClusters):
    - in physics objects
    - not used in physics objects
  - Muons
  - Tracks in regions where Calorimeter/Muon Spectrometer are inefficient
  - Correction for energy lost in dead material

Fake Missing ET

• **Fake muons** can be caused by jet punch-through detected as excess activity in Muon Chambers.
• **Cleaning criteria:** count of muon hits and of muon segments within a cone around jet axes.

• **Missing muons** due to detector features
  • $\eta=0$: holes in Muon Spectrometer for cables, services to Inner Detector & Calorimeter.
  • $|\eta| \sim 1.2$: middle muon station missing for initial data taking
  • $|\eta|>2.7$: no muon coverage
• **use calorimeter and track information** to recover missing muons used in E_T^{miss} calculation
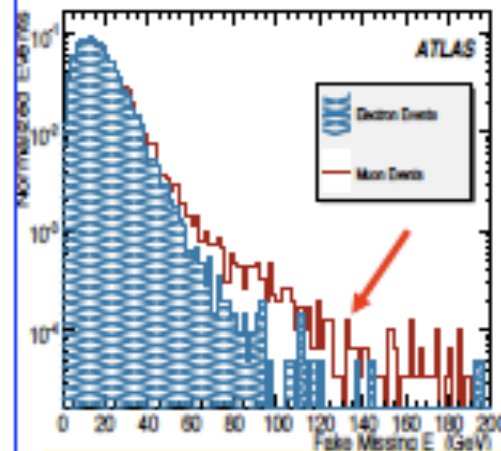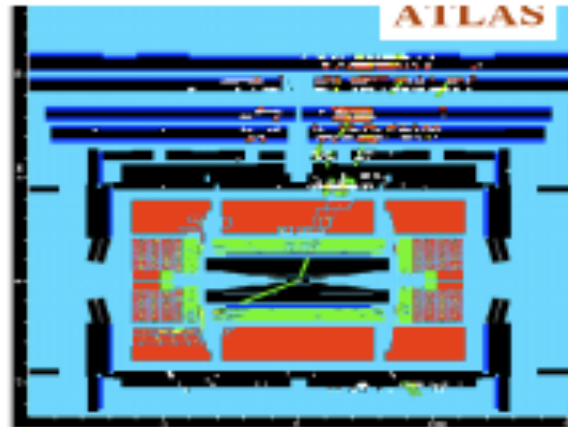
E_T^{miss} Fake in ttbar events in the electron and muon channel:
⇒large tails due to missed or fake muons

$$E_{x,y}^{miss} \text{ Fake} = E_{x,y}^{miss} - E_{x,y}^{miss}\text{True}$$

Fake Missing ET

Fake E_T^{miss} in calorimeter can also be produced by mis-measurements of jets due to cracks, gaps, transition regions used for services.

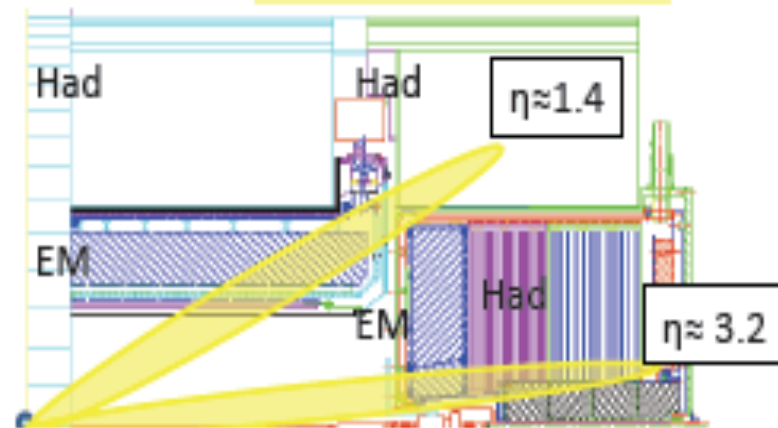Crack* regions: η ≈1.4, 3.2

- Leakage of jets entering 'crack' region 1.3<|η|<1.6 can be detected:
  - looking for large deposits in the outermost layers of the calorimeter
  - checking the E_T^{miss} calculated from tracks found in the Inner Detector that can provide a complementary information
  - checking if E_T^{miss} is closely associated with one of the leading jets in the transverse (φ) plane
- Cleaning cuts based on those criteria could be applied⇒ analysis dependent

Had   Had   η≈1.4

EM   EM   Had   η≈ 3.2

Δφ(jet-E_T^{miss})

Jet 1

E_T^{miss}

Jet 2

Di-jet QCD sample 560 GeV<p_T<1120 GeV

ATLAS   True E_T^{miss}
Before DeltaPhi Cut   Fake E_T^{miss}

ATLAS   True E_T^{miss}
After DeltaPhi Cut   Fake E_T^{miss}
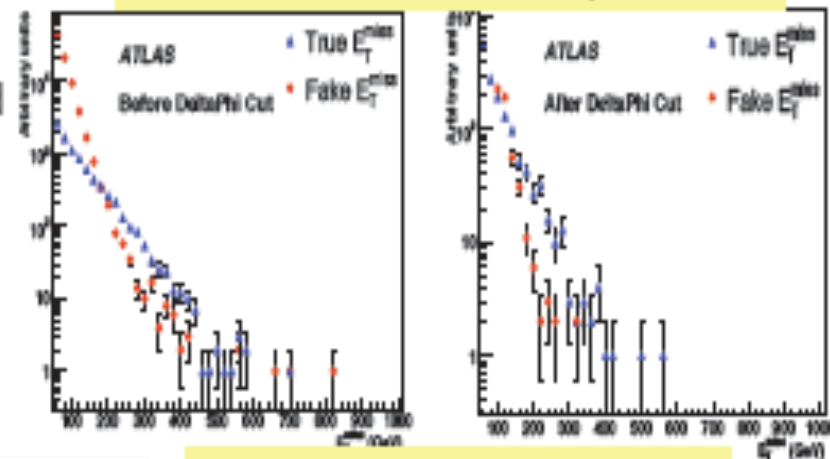
$E_{x,y}^{miss}$ Fake= $E_{x,y}^{miss}$ - $E_{x,y}^{miss}$True   12

Jet energy scale

- **Factorized multi-step approach**
  - Flexibility to understand corrections individually and use different techniques as they become validated with data within a same framework
  - Combination of "in-situ" and Monte Carlo (MC) methods

Hadronic Calibration:
- correct for calorimeter effects: non-compensation, dead material
- ATLAS developped two different strategies: **Global and Local calibration**
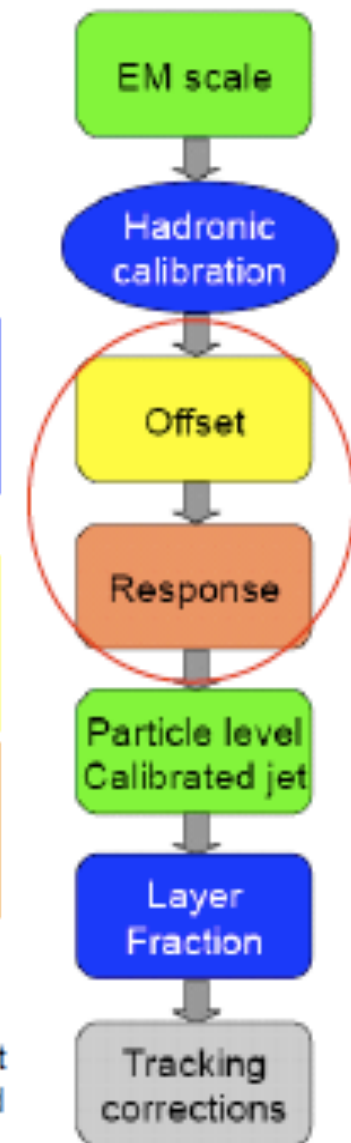
Jet Energy Scale

Offset correction for pile-up:
- subtract the average contribution to the jet energy not originating from the primary interaction
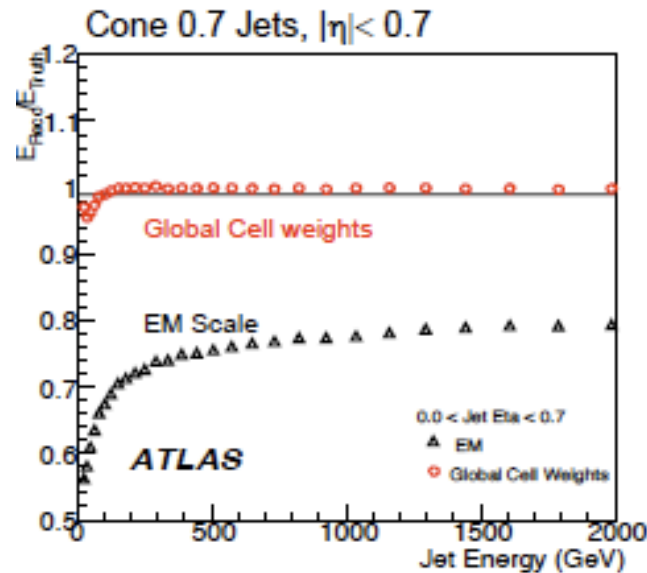
Response correction:
- **Eta intercalibration**: equalization of the jet response as a function of η
- **Absolute energy scale**: in-situ correction from gamma/Z-jet balance

Other optional corrections to improve resolution (scale unchanged):
- **Layer Fraction**: EM-scale jets + layer fraction, exploit longitudinal shower development
- **Tracking corrections**: fraction of jet momentum carried by charged tracks associated with the jet
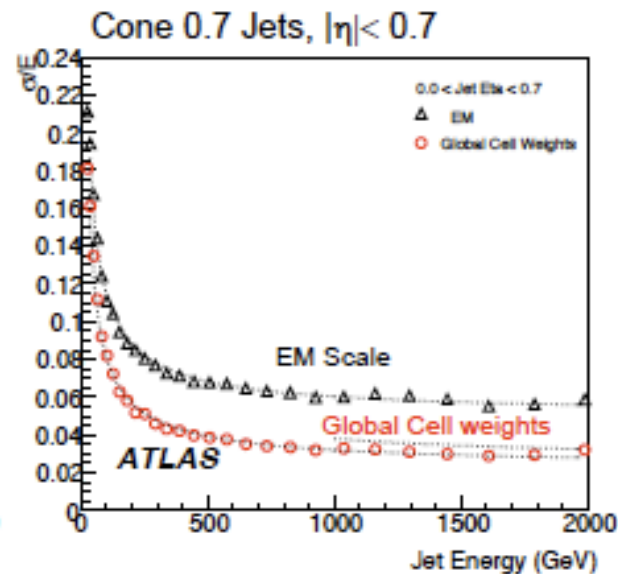
EM scale → Hadronic calibration → Offset → Response → Particle level Calibrated jet → Layer Fraction → Tracking corrections

Jet Reconstruction

Cone 0.7 Jets, |η|< 0.7

Global Cell weights

EM Scale

ATLAS

0.0 < Jet Eta < 0.7
△ EM
○ Global Cell Weights

Jet Energy (GeV)

Cone 0.7 Jets, |η|< 0.7

0.0 < Jet Eta < 0.7
△ EM
○ Global Cell Weights

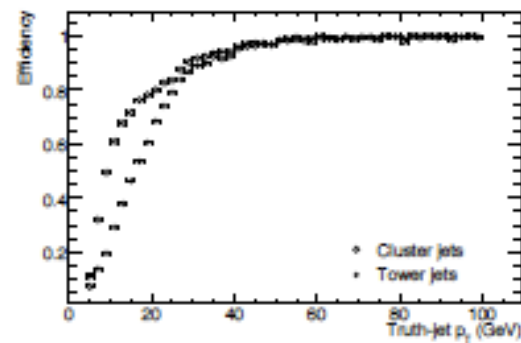EM Scale

Global Cell weights

ATLAS

Jet Energy (GeV)

Jet energy response linearity
- Global Cell weights within 2%
- largest non linearity coming from low energies

Jet energy resolution
- Global Cell weights ~ 4% at high energy

Efficiency

Cluster jets
Tower jets

Truth-jet p$_T$ (GeV)

Purity

Cluster jets
Tower jets

Reconstructed jet p$_T$ (GeV)

Figure 10.76: Efficiency of jet reconstruction in VBF-produced Higgs-boson events as a function of p_T of the truth-particle jet for cone-tower and cone-cluster jets with $\Delta R = 0.7$.
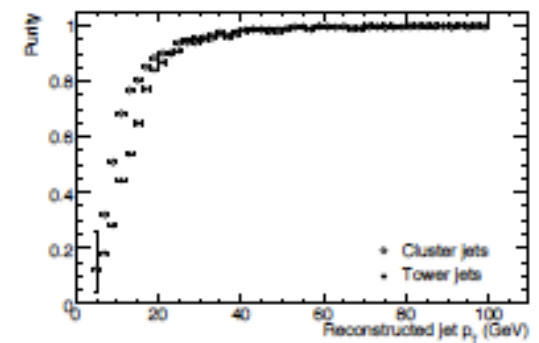
Figure 10.77: Purity of jet reconstruction in VBF-produced Higgs-boson events as a function of p_T of the reconstructed jet for cone-tower and cone-cluster jets with $\Delta R = 0.7$.

Missing ET Reconstruction

Basic E_T^{miss} from all calorimeter cells applying two possible noise suppression approaches:

- from all Cells with $|E|>2\sigma$ noise
- from all Cells inside TopoClusters

$\Rightarrow$ NO calibration, usable since day 1

Final E_T^{miss} obtained adding:

- Calibration step: two different calibrations approaches (coherent with jets):
  - Global cell energy density calibration and local hadron calibration applied
- Contribution from muons: $E_{x,y}^{Muon} = - \sum_{RecMuon} E_{x,y}$
- Correction for energy lost in cryostat between EM and Had calorimeters from jets:

$$E_{jet}^{cryo} = w^{cryo}\sqrt{E_{EM3} \times E_{HAD}}$$
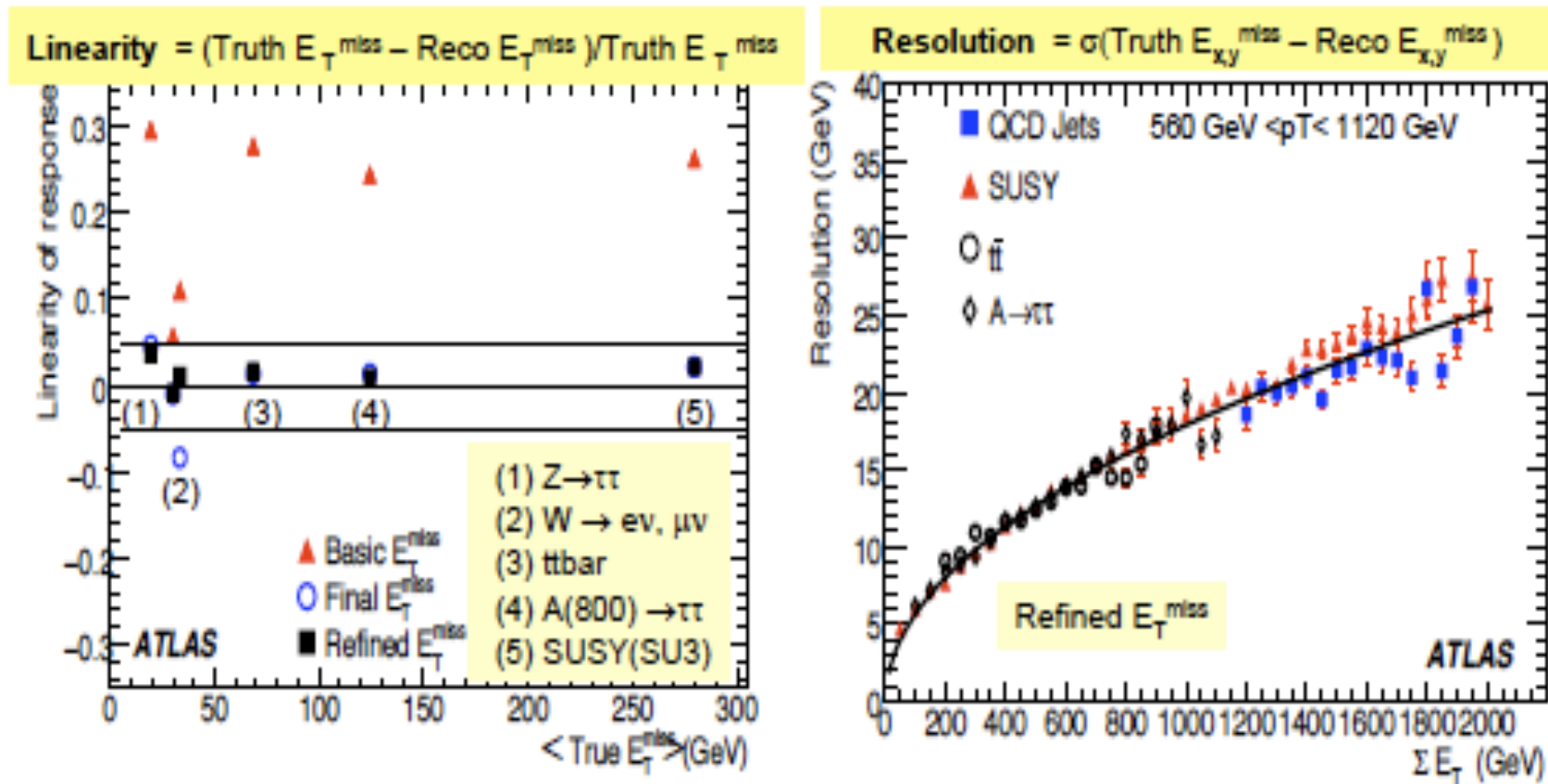
Refined E_T^{miss} original approach by ATLAS based on event signal ambiguity resolution:

- sequential decomposition of reconstructed objects: *electrons, photons, taus, jet, muons* into basic constituents (calorimeter cells or TopoClusters) and veto of multiple contribution to guarantee no double counting in E_T^{miss} calculation
- Calibration weights applied to basic constituents depend on the type of reconstructed object
- Also TopoClusters not associated with any reconstructed objects taken into account

$\Rightarrow$ Most complex schema, usable after validation of reconstructed objects

Missing ET performance

Linearity $= (\text{Truth } E_T^{miss} - \text{Reco } E_T^{miss})/\text{Truth } E_T^{miss}$

Resolution $= \sigma(\text{Truth } E_{x,y}^{miss} - \text{Reco } E_{x,y}^{miss})$

Left plot — axes: Linearity of response vs $<\text{True } E_T^{miss}>$ (GeV)

- ▲ Basic E_T^{miss}
- O Final E_T^{miss}
- ■ Refined E_T^{miss}

(1) $Z \rightarrow \tau\tau$
(2) $W \rightarrow e\nu, \mu\nu$
(3) ttbar
(4) $A(800) \rightarrow \tau\tau$
(5) SUSY(SU3)

ATLAS

Right plot — axes: Resolution (GeV) vs ΣE_T (GeV)

- ■ QCD Jets   560 GeV < pT < 1120 GeV
- ▲ SUSY
- O $t\bar{t}$
- ◊ $A \rightarrow \tau\tau$

Refined E_T^{miss}

ATLAS

E_T^{miss} Refined Calibration provides best performances in terms of Linearity and Resolution (resolution less sensitive to calibration):

- E_T^{miss} Linearity within ~ 3% over wide E_T^{miss} range for different processes
- E_T^{miss} Resolution: mainly depend on ΣET in calorimeters,
  well described by: Resolution $= k * \sqrt{\Sigma E_T}$ (k ~ 0.5)

Flavor tagging

You want to tag these jets a b-jet to reduce backgrounds

Hard fragmentation of b quarks $x_B \sim 70\%$
High mass $m_B \sim 5$ GeV
Lifetime of B hadrons:
$c\tau \sim 470$ μm (mixture $B^+/B^0/B_s$) , ~ 390 μm (Λ_b)
for $E(B) \sim 50$ GeV, flight length ~ 5 mm, $d_0 \sim 500$ μm

→ Spatial tagging:
- Signed impact parameter of tracks (or significance)
- Secondary vertex

Jet axis

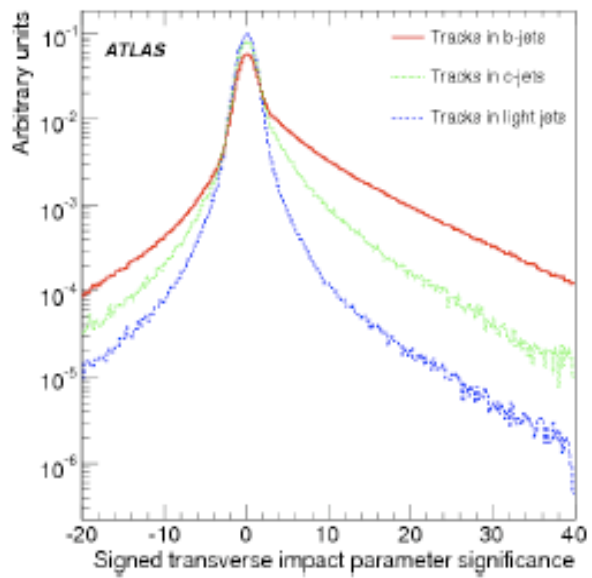Secondary Vertex

$a_0 > 0$

$a_0 < 0$

B

Primary vertex

y

x
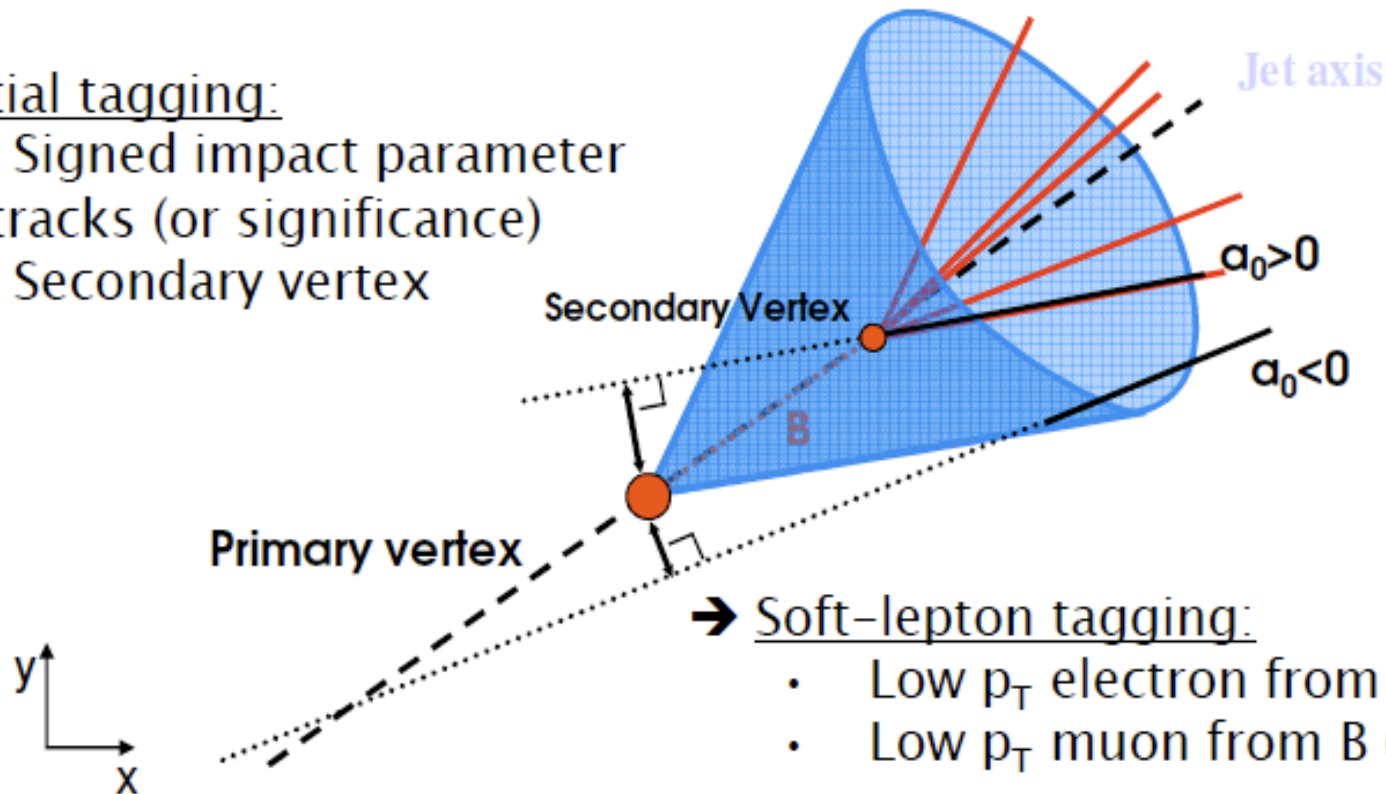
→ Soft–lepton tagging:
- Low p_T electron from B (D)
- Low p_T muon from B (D)

(limited by Br: around 20% each)

Simpler b-taggers

→ Relying on transverse impact parameter:
  → TrackCounting: # of tracks with large d_0/σ
  → JetProb: measuring compatibility of tracks with primary vertex, using a resolution function derived from data: it can be derived already with the 900 GeV data.

→ Relying on secondary vertex:
  – inclusive secondary vertex
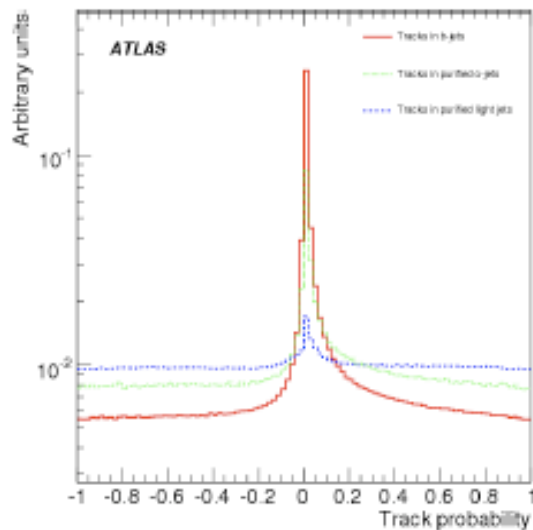
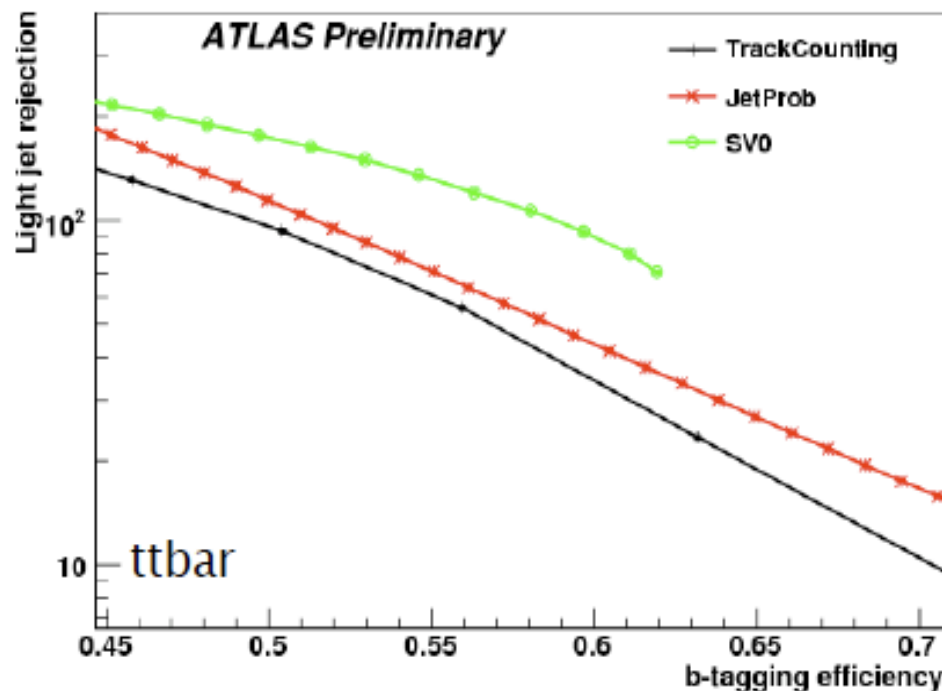Track compatibility with primary vertex

Normalized distance PV–SV
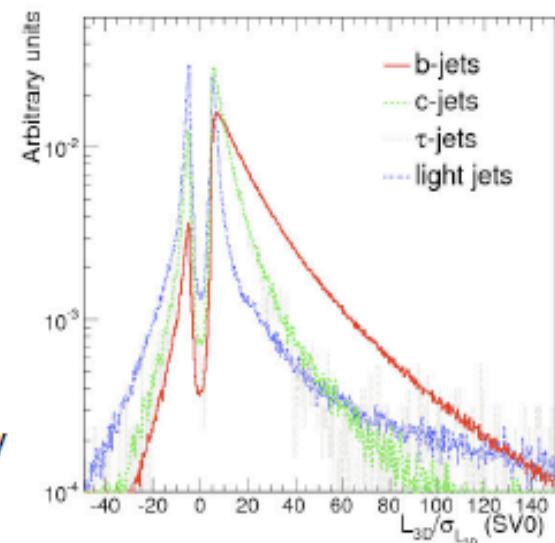
Simpler b-taggers

Test sample:
- 500k ttbar events (10 TeV)
- rather central jets
- average p_T:
  - 70 GeV for b–jets
  - 55 GeV for light jets
- selection: $p_T > 15$ GeV, $|\eta| < 2.5$

Estimators: light jet rejection (inverse of mis–tagging rate) vs b–tagging efficiency.

	$\epsilon_b = 50\%$	$\epsilon_b = 60\%$
TrackCounting	96	38
JetProb	114	44
SV0	173	89

(errors stat.: ±1)

Conclusion

- Particle physics detector design, construction and operation requires a good knowledge of:
    - Basic physics, EM, Relativity, Quantum Mechanics, QED and QCD
    - Basic knowledge of electronics
    - Basic knowledge of software and computing
    - Of course a good background in theoretical physics formalism
- **The rest, data analysis, brings in other requirements**
    - **Particle Identification, event reconstruction, background subtraction**
    - **A good background in statistical methods, for discoveries or setting exclusion limits**